Nuanced role for dendritic cell intrinsic IRE1 RNase in the regulation of antitumor adaptive immunity

Felipe Flores-Santibañez[1,8,9], Sofie Rennen[2,3,9], Dominique Fernandez[1], Clint De Nolf[2], Sandra Gaete[1], Camila Fuentes[4], Carolina Moreno[1], Diego Figueroa[5], Álvaro Lladser[5,6], Takao Iwawaki[7], María Rosa Bono[8], Sophie Janssens[2,3,*] and Fabiola Osorio[1,*]

[1]Laboratory of Immunology and Cellular Stress, Immunology Program, Institute of Biomedical Sciences, Faculty of Medicine, University of Chile, Av. Independencia 1027, 8380453, Santiago, Chile.
[2]Laboratory for ER Stress and Inflammation, VIB Center for Inflammation Research, Technologiepark, Zwijnaarde 71, B-9052, Ghent, Belgium.
[3]Department of Internal Medicine and Pediatrics, Ghent University, De Pintelaan 185, 9000, Ghent, Belgium.
[4]Laboratory of Cancer Immunoregulation, Immunology Program, Institute of Biomedical Sciences, Faculty of Medicine, University of Chile, Av. Independencia 1027, 8380453, Santiago, Chile.
[5]Laboratory of Immunoncology, Fundación Ciencia & Vida, Av Zañartu 1482, 7780272, Santiago, Chile.
[6]Faculty of Medicine and Science, Universidad San Sebastián, Lota 2465, 7510157 Santiago, Chile.
[7]Division of Cell Medicine, Department of Life Science, Medical Research Institute, Kanazawa Medical University, 1-1 Daigaku, Uchinada, Kahoku, Ishikawa 920-0293 Ishikawa, Japan.
[8]Immunology Laboratory, Biology Department, Faculty of Sciences, University of Chile, Las Palmeras 3425, 7800003, Santiago, Chile.
[9] These authors equally contributed to this work.
* Corresponding authors.

Running title: Nuanced role for DC-intrinsic IRE1 RNase in antitumor immunity

Conflict of interest statement: "The authors have declared that no conflict of interest exists."

Correspondence: Fabiola Osorio
Immunology Program
Institute of Biomedical Sciences
Faculty of Medicine
Universidad de Chile
Av. Independencia 1027
Postal code: 8380453
Santiago
Chile
Phone: +56-2-29789503
Email: fabiolaosorio@med.uchile.cl

Sophie Janssens
Laboratory for Endoplasmic Reticulum Stress and Inflammation
VIB Center for Inflammation Research,
Technologiepark 71
B-9052 Zwijnaarde
Ghent
Belgium
Email: sophie.janssens@irc.vib-ugent.be

ABSTRACT

The IRE1/XBP1s axis of the unfolded protein response (UPR) plays divergent roles in dendritic cell (DC) biology in steady state versus tumor contexts. Whereas tumor associated DCs show dysfunctional IRE1/XBP1s activation that curtails their function, the homeostasis of conventional type 1 DCs (cDC1) in tissues requires intact IRE1 RNase activity. Considering that cDC1s are key orchestrators of antitumor immunity, it is relevant to understand the functional versus dysfunctional roles of IRE1/XBP1s in tumor DC subtypes. Here, we show that cDC1s constitutively activate IRE1 RNase within subcutaneous B16 melanoma and MC38 adenocarcinoma tumor models. Mice lacking XBP1s in DCs display increased melanoma tumor growth, reduced T cell effector responses and accumulation of terminal exhausted $CD8^+$ T cells. Transcriptomic studies revealed that XBP1 deficiency in tumor cDC1s decreased expression of mRNAs encoding XBP1s and regulated IRE1 dependent decay (RIDD) targets. Finally, we find that the dysregulated melanoma growth and impaired T cell immunity noticed in XBP1 deficient mice are attributed to RIDD induction in DCs. This work indicates that IRE1 RNase activity in melanoma/MC38-associated DCs fine tunes aspects of antitumor immunity independently of XBP1s, revealing a differential role for the UPR axis that depends on the DC subtype and cancer model.

Keywords: Dendritic cells, immunity, IRE1, melanoma, unfolded protein response.

ABBREVIATIONS

BM: bone marrow
cDC: conventional DC
cDC1: type 1conventional DC (XCR1$^+$ DC)
cDC2: type 2conventional DC (CD11b$^+$ DC)
DC: dendritic cell
DEG: Differentially expressed gene
ER: endoplasmic reticulum
ERAI: ER stress-activated indicator
Flt3L: FMS-related tyrosine kinase 3 ligand
FP: fluorescent protein
GSEA: Gene set enrichment analysis
IRE1: inositol-requiring enzyme 1 alpha
KO: Knock-out
MdC: Myeloid derived Cell
RIDD: regulated IRE1-dependent decay
ROS: reactive oxygen species
TAM: tumor-associated macrophages
TCR: T cell receptor
TdLN: Tumor draining lymph node
UPR: unfolded protein response
XBP1s: spliced XBP1
XBP1u: unspliced XBP1

INTRODUCTION

A crucial arm of antitumor immunity relies on effective activation of tumor specific cytotoxic CD8⁺ T cells endowed with the ability to eliminate cancer cells. This process is critically dependent on type 1 conventional dendritic cells (cDC1), which excel in cross-presentation of tumor-associated antigens (1–3), secrete soluble factors that potentiate CD8⁺ T cell function (2, 4–7), and prevent the generation of terminal exhausted CD8⁺ T cells committed to irreversible dysfunctional phenotypes in tumors (8). Tumor cDC1 infiltration correlates with improved prognosis (2, 5, 9) and better response to immune checkpoint blockade (ICB) therapy (9–12). Besides, therapeutic strategies expanding/activating tumor cDC1s have shown promising results in clinical trials (11, 13, 14). Additional DC subsets such as type 2 DCs (cDC2s), and a novel DC activation state termed 'mregDCs' (mature DCs enriched in immunoregulatory molecules) can also boost antitumor CD4⁺ and CD8⁺ T cell responses (7, 15–17), indicating that cDCs are interesting candidates in immunotherapy. However, the molecular mechanisms safeguarding the function of these cells in tumors have not been fully elucidated.

An emerging intracellular pathway regulating DC biology is the inositol-requiring enzyme 1 alpha (IRE1) branch of the unfolded protein response (UPR), which is an adaptive cellular response maintaining the fidelity of the cellular proteome (18). Upon endoplasmic reticulum (ER) stress, the endoribonuclease (RNase) domain of IRE1 splices *Xbp1* mRNA, generating the transcription factor XBP1 spliced (XBP1s), master regulator of protein folding and ER biogenesis (18–20). The IRE1 RNase domain can also promote the degradation of a subset of mRNAs/miRNAs in a process known as 'regulated IRE1-dependent decay' (RIDD) (21), which is a mechanism beginning to be understood in pathological settings including metabolism, inflammation and cancer (22–24).

In steady state, IRE1 regulates cDC homeostasis via constitutive activation of its RNase domain, a feature noticed in cDC1s across several tissues (25, 26). Furthermore, cDC1s are markedly sensitive to perturbations in the IRE1/XBP1s axis, as genetic loss of the transcription factor XBP1 alters proteostatic programs and counter activates the RIDD branch, which mediates the decay of various mRNAs involved in integrin expression, ER to golgi transport and antigen presentation, among others (25, 26). The selectivity of the IRE1/XBP1s axis in cDC1s is underscored in microarray studies of XBP1 deficient cells, which change the transcriptomic landscape of cDC1s but not cDC2s (26). As such, cDC1s opt the IRE1/XBP1s axis for proper function in steady state, but it is unclear if the pathway displays similar roles in cDC1s infiltrating tumors. This is a relevant question, as reported work shows that metabolically stressed tumors elicit maladaptive UPR activation in certain tumor immune cells (including DCs), which reprograms their phenotype towards dysfunctional states that promote tumor growth (27, 28). For instance, DCs infiltrating ovarian cancer (typified by expression of the cDC2/monocyte marker $CD11b^{+}$ (29)) display persistent IRE1/XBP1s activation that triggers aberrant intracellular lipid accumulation, resulting in impaired immunostimulatory functions and leading to tumor progression (30). Thus, these data suggest that IRE1 may play different, or even opposite roles in DC biology depending on the subtype or the inflammatory context. As such, a correct delineation of the role of the enzyme in tumor cDCs is required to understand if intervention of this UPR branch can be targeted for potential cancer therapies.

In this work, we study the role of IRE1/XBP1s in DCs by focusing on two immunoresponsive tumor models: subcutaneous mouse B16/B78 melanoma and MC38 colon adenocarcinoma (2, 10). We identified that cDC1s display constitutive IRE1 RNase activity in tumors, which follows a lineage-intrinsic trait not influenced by the tumor microenvironment. In contrast to previous reports (30), deletion of XBP1 in DCs did not

decrease tumor burden. Rather, XBP1 deficiency in DCs resulted in a moderate increase of tumor growth, lower frequencies of intratumoral effector T cells, and accumulation of terminal exhausted TIM-3^{+}CD8^{+} cells in the melanoma model. Transcriptomic studies revealed that XBP1 deficient tumor cDC1s downregulate proteostatic processes and decrease the expression of mRNAs encoding XBP1s and regulated IRE1 dependent decay (RIDD) targets. Importantly, animals bearing double deletion of IRE1 RNase and XBP1 in DCs display normal tumor growth and adaptive immunity in the melanoma model, highlighting a role for IRE1 RNase hyperactivation in fine tuning aspects of antitumor immunity via DCs.

RESULTS

cDC1s constitutively activate IRE1 RNase in subcutaneous melanoma and MC38 colon carcinoma tumors

The tumor microenvironment contain activators of the IRE1/XBP1s axis that are detected by immune cells (27, 30–32). To identify relevant cell types activating IRE1 RNase in tumors, we analyzed the immune composition of B16 tumors of ERAI mice, a mouse strain that reports IRE1 RNase activity through expression of Venus Fluorescent Protein (VenusFP) fused with the sequence of *Xbp1s* mRNA (33) (validated in (25, 26, 31)). To allow unsupervised identification of IRE1 RNase cellular targets, we devised a 17-color flow cytometry panel and data was visualized on a *t*-distributed stochastic neighbor embedding (*t*-SNE) map. Cells were grouped into populations by DBScan-guided automated clustering (Fig. 1A-B, Supp. Fig. 1A), which identified 15 cell clusters that included $CD8^+$ T cells, $CD4^+$ T cells, monocyte-derived cells (MdCs), MHC-II-expressing MdCs, NK cells, NKT cells, B cells, neutrophils and cDC1s. As expected (17), cDC2s and tumor associated macrophages (TAMs) (clusters 4 and 6) showed a degree of heterogeneity and convergence. Also, our analysis revealed two undefined clusters based on surface marker expression; Cluster 11: $CD4^+$ $CD11c^+$ $CD26^+$, and Cluster 14: $CD3^+$ $CD4^+$ $CD11b^{int}$ $F4/80^+$ $MHC\text{-}II^{high}$ $CD11c^{int}$ $CD26^{high}$.

Next, IRE1 RNase activity from the ERAI reporter mice line was determined in the clusters of the t-SNE plot (Fig. 1C-D). Data indicated that among $CD45^+$ hematopoietic cells, cDC1s represented the population with highest fluorescence intensity of VenusFP (Fig 1C-D, cluster 15). Additional immune cells including cDC2s, MdC, $MHC\text{-}II^+$MdC, TAM, neutrophils, NK cells and cells from cluster 11 also showed noticeable VenusFP induction, albeit at lower levels than cDC1s; whereas $CD4^+$ T cells, $CD8^+$ T cells and B cells showed little or no induction of VenusFP compared to cells from control animals (Fig 1D). Manual

gating analysis (Fig. 1E-F, Supp. Fig. 2A) confirmed that the mean fluorescence intensity (MFI) of VenusFP in melanoma-associated cDC1s was higher than additional myeloid and lymphoid cells (Fig. 1E-F). Notably, similar results were observed in cDC1s infiltrating MC38 tumors (Supp. Fig. 1B). Finally, these data was confirmed by PCR for endogenous *Xbp1* spliced and unspliced forms from tumor cDC1s isolated from wild type (WT) animals implanted with the B16-FLT3L melanoma cell line (which expresses the DC-differentiation factor FMS-like tyrosine kinase 3 ligand (FLT3L) (11, 34)). Data in Fig. 1G-H showed that tumor cDC1s expressed marked levels of *Xbp1s*, which was even superior to the levels noticed in bone-marrow derived DCs (BMDC) stimulated with the pharmacological UPR inducer tunicamycin. Altogether, these data indicate that cDC1s display prominent activation of the IRE1/XBP1s axis in tumors.

We next interrogated whether the augmented IRE1 RNase activity observed in tumor cDC1s is a lineage-intrinsic signature or if it is a feature imposed by the tumor microenvironment. We quantified the VenusFP MFI of cDC1s directly exposed to the tumor (tumor cDC1 and migratory cDC1s of the tumor draining lymph node (TdLN)), versus TdLN resident cDC1s, which do not access to the tumor site (gating strategy in Supp. Fig. 2B) (35). Data depicted in Fig. 1I indicates that tumor cDC1s express lower levels of VenusFP than resident cDC1s, indicating that tumor exposure does not increase IRE1 RNase activity in these cells. Similar observations were made for cDC2s (Fig 1I). In fact, cDC1s infiltrating MC38 tumors express markedly lower levels of VenusFP than spleen cDC1s (Supp. Fig. 1C). Of note, this observation was not replicated in monocytes, which express higher VenusFP levels in the tumor compared to the spleen (Fig 1J). Altogether, these data suggest that IRE1 RNase activation in tumor cDCs is a stable lineage intrinsic trait not driven by the microenvironment.

XBP1 deletion in CD11c-expressing cells results in increased melanoma tumor growth

To gain insights on the role of XBP1 in DCs during melanoma tumor growth, we studied the *Itgax*-Cre x *Xbp1*$^{fl/fl}$ mice (36, 37), referred to as 'XBP1$^{\Delta DC}$' mice, in which exon 2 of *Xbp1* is excised in CD11c-expressing cells, resulting in absence of the transcription factor in DCs (26). These animals were compared to control littermates (*Xbp1*$^{fl/fl}$ animals with no expression of Cre), referred to as 'XBP1^{WT}' mice. XBP1^{WT} and XBP1$^{\Delta DC}$ mice were implanted with the B78-ChOVA melanoma line, a B16 variant that expresses the ovalbumin (OVA) antigen and mCherry fluorescent protein (2). Data in Figure 2A-B indicate that XBP1$^{\Delta DC}$ mice showed moderate but noticeable acceleration of tumor growth and significantly larger tumor size than tumors from XBP1^{WT} mice on day 12 post implantation (80.44 ± 8.927 vs 56.56 ± 6.174 mm^3, p = 0.0312, mean ± s.e.m.) (Fig. 2B). As a second tumor model, we also analyzed growth of subcutaneous MC38 murine colon adenocarcinoma tumors, which also showed a trend towards increased tumor growth in XBP1$^{\Delta DC}$ mice, but without reaching statistical significance (Supp. Fig. 3A-C).

To understand if XBP1 deficiency in the CD11c compartment resulted in altered cell recruitment, we quantified the immune cell composition at the melanoma tumor site. XBP1^{WT} and XBP1$^{\Delta DC}$ mice show similar numbers of CD45$^+$ cells (Fig. 2C), and comparable composition of tumor cDC1/cDC2 and resident and migratory cDC1/cDC2s in the TdLN (Fig. 2D-E). Furthermore, conditional *knock-out* and control animals also showed comparable frequencies of myeloid and lymphoid cells (Fig. 2F-H). These data indicate that XBP1s expression by DCs infiltrating melanoma and MC38 tumor does not promote tumor progression. Rather, loss of XBP1s in DCs leads to increased melanoma tumor growth by mechanisms that are independent of immune cell recruitment.

XBP1 deletion in CD11c-expressing cells results in impaired antitumor T cell responses and disbalanced precursor/terminal exhausted T cell ratio

We next focused our analysis on DC function. It was recently identified a conserved immunoregulatory transcriptional program activated by tumor DCs based on the co-expression of the molecules CD40 and PDL-1 plus the cytokine IL-12 (15). Our analysis revealed that tumor and migratory cDC1/cDC2s from XBP1$^{\Delta DC}$ mice express normal levels of these molecules (Fig. 3A, Supp. Fig. 4A). We also studied bone marrow cDC1s generated upon culture with OP9-DL1 stromal cell line plus FLT3L (reported in (38, 39)). We found that bone marrow cDC1s from XBP1$^{\Delta DC}$ mice produce lower levels of IL-12 in unstimulated conditions (Fig 3B, Supp. Fig. 4B). However, upon tumor exposure, expression of IL-12 was comparable between XBP1 sufficient and deficient cDC1s. We conclude that XBP1s regulate certain parameters of DC activation in steady state that are restored upon tumor encounter.

Considering previous findings showing that XBP1s deficient cDC1s have impaired cross-presentation abilities in steady state (26), we interrogated if the mice line was able to cross-present melanoma-associated antigens. We implanted B78ChOVA tumors in XBP1^{WT} and XBP1$^{\Delta DC}$ mice and quantified the presence of endogenous OVA-specific CD8^{+} T cells using H-2K^{b}-OVA$_{257-264}$ tetramers. XBP1^{WT} and XBP1$^{\Delta DC}$ contained similar frequencies of OVA-specific CD8^{+} T cells in tumors and TdLN (Fig. 3C-D, Supp. Fig 4C). A similar response was obtained when tracking proliferation/early activation of CD8^{+} T cells isolated from pmel mice, which possess transgenic CD8^{+} T cells bearing a TCR selective for the melanoma-associated antigen gp100 (40) (Supp. Fig. 4D-E). Thus, we conclude that XBP1 deletion in tumor-associated CD11c^{+} cells does not prevent cross-presentation of melanoma-associated antigens.

We next investigated the quality of the antitumor T cell response evoked in XBP1$^{\Delta DC}$ mice. As a measure of T cell quality, we analyzed cytokine producing T cells from tumors of XBP1^{WT} and XBP1$^{\Delta DC}$ mice. Tumors from XBP1$^{\Delta DC}$ mice contained lower frequencies of IFN-γ-producing and TNF-producing CD8$^+$ T cells, which also resulted in decreased frequencies of double producers IFN-γ$^+$TNF$^+$ CD8$^+$ T cells and triple producers IFN-γ$^+$TNF$^+$IL-2$^+$ CD8$^+$ T cells (Fig. 3E-F). These observations were also noticed in the CD4$^+$ T cell compartment, as reduced frequencies of IFN-γ$^+$ CD4$^+$ T cells and IFN-γ$^+$ TNF$^+$ CD4$^+$ T cells were found in tumors from XBP1$^{\Delta DC}$ mice (Fig. 3G). As such, absence of XBP1 in CD11c-expressing cells results in decreased CD8$^+$ and CD4$^+$ T cell effector function in melanoma tumors. Analysis of the MC38 model showed that whereas the CD8$^+$ T cell response was not affected, there was a significant reduction in the frequencies of IFN-γ-producing and IFN-γ/ TNF-producing CD4$^+$ T cells (Supp. Fig. 4F-G).

Impaired cytokine production is a hallmark of CD8$^+$ T cell exhaustion in cancer (41, 42), a process characterized by a progressive loss of function that culminates with the generation of terminal exhausted TIM-3$^+$CD8$^+$ T cells unable to control tumor growth (42). TIM-3$^+$CD8$^+$ T cells do not proliferate, are unresponsive to anti-PD1 therapy (41, 43) and originate from 'precursor exhausted' CD8$^+$ T cells, a T cell state characterized by the expression of the transcription factor TCF-1 (termed 'TCF1$^+$CD8$^+$ T cells'), which retain proliferative potential and can be reinvigorated through anti-PD1 therapy (41, 43, 44). We determined the presence of intratumoral TCF-1$^+$CD8$^+$ T cells and TIM-3$^+$CD8$^+$ T cells in melanoma tumors from XBP1$^{\Delta DC}$ mice and control animals. Tumors from XBP1$^{\Delta DC}$ mice show decreased infiltration of TCF-1$^+$CD8$^+$ T cells and increased proportions of TIM-3$^+$CD8$^+$ T cells compared to tumors from control animals (Figure 3H-I). Additionally, TIM3$^+$ CD8$^+$ T cells from XBP1^{WT} and XBP1$^{\Delta DC}$ mice display a *bona-fide* terminal exhausted phenotype, with elevated levels of CD39, TOX and granzyme B (Supp. Fig. 4H). These

findings are consistent with data depicted in figure 3E-F showing lower frequencies of polyfunctional cytokine-producing $CD8^+$ T cells in tumors from $XBP1^{\Delta DC}$ mice, which is an attribute of precursor exhausted $TCF\text{-}1^+CD8^+$ T cells (41). Altogether, our data shows that XBP1s in the $CD11c^+$ compartment coordinates the balance of $CD8^+$ T cell profiles in melanoma.

Tumor cDC1s from $XBP1^{\Delta DC}$ mice display signs of RIDD

Thus far, our data indicate that XBP1s expression in DCs modulates melanoma tumor growth and the balance of effector and exhausted T cell subsets. However, it is unclear if these processes depend on XBP1s-transcriptional activity, as previous work demonstrated that XBP1s deficiency leads to hyperactivation of IRE1 RNase and RIDD in steady state cDC1s (25, 26). Thus, we interrogated if XBP1 deficiency also resulted in increased IRE1 RNase activity in tumor cDC1s (Fig 4A). We measured expression of *Xbp1* spliced/unspliced mRNA in tumor cDC1s from control and $XBP1^{\Delta DC}$ mice. Although $XBP1^{\Delta DC}$ cDC1s are unable to synthesize XBP1s protein, these cells still generate *Xbp1* mRNA bearing the IRE1 cleavage sites, which serves as an assay to monitor IRE1 RNase activity (26). Data in Figure 4B show that tumor cDC1s isolated from $XBP1^{\Delta DC}$ mice express marked levels of *Xbp1s* mRNA compared to control counterparts, which is an indicative sign of IRE1 RNase hyperactivation.

To determine RIDD on protein level in tumor DCs, we determined surface expression of the integrin CD11c, a dimeric partner of *Itgb2* (coding the integrin CD18), which is a reported mRNA substrate of IRE1 RNase (26). CD11c surface expression depends on RIDD-mediated degradation of *Itgb2* mRNA and therefore, it can be used as a surrogate marker for RIDD activity. Data in Fig. 4C show that tumor cDC1s from $XBP1^{\Delta DC}$ express lower surface levels of CD11c than control counterparts, confirming RIDD induction on

protein level. Similar effect was observed in cDC1 subsets from the TdLN (Fig 4D). These data show that XBP1-deficient cDC1s display signs of RIDD in melanoma tumors. Interestingly, additional APCs such as tumor cDC2s and TAM from XBP1$^{\Delta DC}$ mice showed a modest but noticeable reduction in CD11c expression (Fig. 4C), suggesting that these cells may also induce RIDD upon XBP1 loss, albeit at lower extent than cDC1s.

Gene expression profiles of tumor cDC1s deficient for IRE1 RNase and XBP1

Given that XBP1 deficient cDC1s show signs of RIDD at the tumor site, we analyzed the transcriptomic signature downstream of IRE1 RNase in melanoma-infiltrating cDC1s. To identify specific XBP1-dependent and RIDD-dependent targets, we carried out a parallel analysis of the transcriptome of tumor cDC1s deficient for XBP1, or double deficient for the RNase domain of IRE1 and XBP1. To generate double *knock-out* animals for the IRE1 RNase and XBP1 in CD11c-expressing cells, we crossed XBP1$^{\Delta DC}$ mice with *Ern1*$^{fl/fl}$ mice, which bear loxP sites flanking exon 20 and 21 of the *Ern1* gene and generates a truncated IRE1 isoform lacking the RNase domain (45) (referred to as "XBP1$^{\Delta DC}$/IRE1^{trunc}DC mice"). As such, XBP1$^{\Delta DC}$ mice lack the transcription factor and activate RIDD, whereas double deficient XBP1$^{\Delta DC}$/IRE1^{trunc}DC mice lack both XBP1s and RIDD (Supp. Fig 5A-C). With this strategy, XBP1s target genes are identified as transcripts that are downregulated in tumor cDC1s from both XBP1$^{\Delta DC}$ and XBP1$^{\Delta DC}$/IRE1^{trunc}DC mice. In contrast, RIDD-dependent transcripts are recognized as mRNAs that decrease their expression in XBP1-deficient tumor cDC1s, but which expression is restored in XBP1$^{\Delta DC}$/IRE1^{trunc}DC animals.

Tumor cDC1s were isolated by cell sorting from B16 melanoma tumors of control, XBP1$^{\Delta DC}$ or XBP1$^{\Delta DC}$/IRE1^{trunc}DC mice and the transcriptome was analyzed by bulk RNA sequencing (RNA-seq). 51 differentially expressed genes (DEG) were identified among XBP1$^{\Delta DC}$ or XBP1$^{\Delta DC}$/IRE1^{trunc}DC cDC1s (adjusted p-value < 0.05 and |Fold Change| > 1.5)

(Fig. 5A). Biological pathway enrichment analysis using Gene Ontology (GO) knowledgebase revealed that a large proportion of DEGs are constituents of the response to misfolded proteins and transport and localization of ER proteins (see Biological Process, Fig. 5B). There was also an overrepresentation of protein disulfide-isomerases (see Molecular Function, Fig. 5B) and on intracellular localization level, most deregulated genes encoded ER proteins (see Cellular Component, Fig. 5B). Next, we analyzed the DEGs per mice line, which clustered these genes into three main groups: (1) genes upregulated in XBP1-deficient and IRE1 RNase/XBP1-deficient tumor cDC1s; (2) genes downregulated in both XBP1-deficient and IRE1 RNase/XBP1-deficient tumor cDC1s (XBP1s targets); and (3) genes downregulated exclusively in XBP1-deficient tumor cDC1s (potential RIDD targets) (Fig. 5A). In group (1), we identified five transcripts including *Hspa5* which encodes BiP, a chaperone induced upon UPR activation (46). This finding indicates that XBP1-deficient and IRE1 RNase/XBP1-double deficient tumor cDC1s show signs of ER stress (Fig. 5A). We also identified *Cox6a2* (subunit of cytochrome C oxidase), which was previously identified as an upregulated gene in XBP1-deficient cDC1s (26). Transcripts in group (2) include protein disulfide isomerases (*Erp44, Txndx11, Txndc5, P4hb*) chaperones (*Dnajb9/Hyou1*); glycosylation proteins (*Rpn1, Alg2, Serp1*), proteins involved in transport to the ER (*Sec61a1, Sec61b, Spcs2, Spcs3, Ssr3*) and from the ER to Golgi (*Bet1, Surf4*) (Fig. 5A). Additional canonical XBP1s targets (*Stt3a* and *Edem2)* were identified when the cut off value was set below 1.5-fold (Supp. Fig 6A). Gene Set Enrichment Analysis (GSEA) revealed that the transcriptome of both XBP1$^{\Delta DC}$ and XBP1$^{\Delta DC}$/IRE1^{trunc}DC tumor cDC1s were depleted of targets related to protein glycosylation, ER to Golgi transport, protein localization to the ER and lipid biosynthesis (Fig 5C-D).

Finally, group (3) includes the canonical RIDD substrates *Bloc1s1*, *St3gal5* (21), *Itgb2* (26), plus a subset of transcripts with heterogeneous functions (Fig. 5A) that range from lipid synthesis and metabolism members (*St3gal5, Gm2a, Abca2*), Ca^{+2} homeostasis (*Stim2, Pkd1*), protein folding (*Qsox1, Mlec*), a steroid binding receptor (*Paqr7*), an amino acid transporter (*Slc1a5*) , a member of the nuclear pore complex (*Nup210*), an E3-ubiquitin ligase (*Rnf130*), signaling receptors in immunity and development (*Fcrla*, *Notch4*, respectively) to *Eif2ak3,* which encodes the UPR transducer PERK. Consistent with the functional heterogeneity of RIDD targets, GSEA did not reveal differences at the level of biological processes between $XBP1^{\Delta DC}$ and $XBP1^{\Delta DC}/IRE1^{trunc}DC$ cDC1s (Fig 5C-D). Even though some processes such as antigen processing and presentation and cell-redox homeostasis are downregulated exclusively in tumor cDC1s from $XBP1^{\Delta DC}$ mice (thereby suggesting RIDD dependency), these processes display low enrichment scores. To sum up, these data indicate that tumor cDC1s from $XBP1^{\Delta DC}$ mice display an altered XBP1s transcriptional program related to protein homeostasis and folding, and counter activate RIDD. Using GSEA and reported XBP1s-target and RIDD-target gene datasets (31, 47) we confirmed downregulation of the canonical XBP1s transcription program in both $XBP1^{\Delta DC}$ cDC1s and double deficient $XBP1^{\Delta DC}/IRE1^{trunc}DC$ cDC1s (Fig 5E-F, Supp. Fig. S6B), whereas RIDD-dependent targets are predominantly downregulated in $XBP1^{\Delta DC}$ cDC1s (Fig 5E-F, Supp Fig. S6B). Finally, our findings reveal that melanoma-infiltrating cDC1s do not show signs of dysfunctional XBP1s activity, as genes related to triglyceride biosynthesis that are associated with diminished DC function in other cancer settings are not downregulated upon XBP1s or IRE1 RNase loss (Supp. Fig. 6C-D) (30). Taken together, these results demonstrate that XBP1 deficiency in tumor cDC1s impairs transcriptomic programs associated with the maintenance of proteostasis and induces RIDD.

434 **RIDD activation in DCs accounts for the changes related to tumor growth and**
435 **dysregulated antitumor T cell immunity noticed in XBP1$^{\Delta DC}$ mice**

436 Our observations raise the question as to whether the increased tumor growth and T cell
437 dysregulation noticed in XBP1$^{\Delta DC}$ mice is due to XBP1s- or RIDD-dependent outputs in
438 DCs. To address this issue, we implanted the B78ChOVA cell line in control and
439 XBP1$^{\Delta DC}$/IRE1^{trunc}DC animals (Fig. 6A-B), in which RIDD is abolished (Supp. Fig. 5A-C).
440 Remarkably, in contrast to the observations noticed in XBP1$^{\Delta DC}$ mice (Fig. 2A), the tumor
441 size of animals lacking both XBP1 and IRE1 RNase in DCs was comparable to that
442 observed in control animals (41.78 ± 9.033 vs 53.90 ± 12.36 mm^3, p=0.42, mean ± s.e.m.)
443 (Fig. 6B), indicating that RIDD activation in CD11c-expressing cells accounts for the
444 increased tumor growth. Furthermore, we examined whether the reduced frequencies of
445 cytokine producing CD8$^+$ T cells and the disbalance between TCF-1$^+$/TIM-3$^+$ CD8$^+$ T cells
446 noticed in XBP1$^{\Delta DC}$ mice are also dependent on RIDD. Analysis of tumor-infiltrating CD8$^+$
447 T cells revealed no differences in the frequencies of IFN-γ producing CD8$^+$T cells, TNF
448 producing CD8$^+$T cells, IL-2 producing CD8$^+$T cells, nor in the proportion of double or
449 triple cytokine producers between XBP1$^{\Delta DC}$/IRE1^{trunc}DC mice and control animals (Fig.
450 6C-D). Similar results were observed for IFN-γ producing or double IFN-γ/ TNF-α
451 producing CD4$^+$ T cells (Fig. 6E). In addition, analysis of the composition of precursor-
452 exhausted/terminal exhausted T cells revealed similar infiltration of TCF-1$^+$/TIM-3$^+$ CD8$^+$
453 T cells in melanoma tumors from XBP1$^{\Delta DC}$/IRE1^{trunc}DC mice versus control animals (Fig.
454 6F-G), indicating that IRE1 RNase activity in DCs accounted for the accumulation of
455 dysfunctional CD8$^+$ T cells in melanoma. Altogether, these data indicates that
456 hyperactivation of the RNase domain of IRE1 in DCs fine tunes melanoma tumor growth
457 and antitumor T cell immunity.

458

DISCUSSION

The IRE1/XBP1s axis has emerged as a critical regulator of immunity and cancer (27, 48, 49). The differential mechanisms by which IRE1 signaling integrates the intensity and duration of ER stress to regulate cell fate is particularly noticed in the immune system, with cells such as cDC1s, B cells, NK cells and eosinophils that opt for an intact IRE1/XBP1s axis to maintain cellular health (25, 31, 50, 51), or cells including TAM/MdCs or intratumoral T cells, which acquire dysfunctional phenotypes upon enforced activation of the UPR sensor (27, 32, 52).

Here, we report that loss of XBP1 in CD11c-expressing cells results in increased melanoma tumor growth, decreased frequencies of cytokine-producing T cells and accumulation of terminal exhausted TIM-3^{+}CD8^{+} T cells. Notably, this effect is abrogated in XBP1$^{\Delta DC}$/IRE1^{trunc}DC mice, demonstrating that IRE1 RNase-dependent, XBP1s-independent outputs account for the dysregulated antitumor immunity in melanoma. We also observe a milder phenotype in the MC38 model, suggesting that different tumor models differentially regulate the IRE1/XBP1s axis in DCs.

The results presented in this work contrast with previous studies demonstrating that persistent IRE1/XBP1s activation in tumor DCs curtails their antitumor function. In ovarian cancer, the same XBP1$^{\Delta DC}$ mice line show marked inhibition of tumor progression and improved antitumor immunity (30). One possibility accounting for these differences may be related to the different composition of DCs infiltrating these cancer models. In ovarian cancer models, tumor-associated DCs are spontaneously immunosuppressive (53) and in fact, whereas depletion of CD11c^{+} cells delays ovarian cancer progression in later stages (54), the same process curtails CD8^{+} T cell priming in melanoma (55). Furthermore, XBP1 deficiency in ovarian cancer DCs does not lead to RIDD activation (30), which contrasts to the evidence presented in this work. Thus, as result of these

combined data, we must consider that the outcome of the IRE1 outputs in tumor DCs may drastically differ depending on the DC subset and the cancer type. In fact, data presented here show that animals lacking both XBP1 and IRE1 RNase in DCs display normal melanoma tumor growth and T cell immunity, indicating that the deletion of an entire branch of the UPR in DCs does not have a predetermined role across different tumor types. These results complement existing literature and may be relevant for building a comprehensive understanding on future manipulation of the IRE1/XBP1s axis in cancer.

In addition, even though we use a genetic model of XBP1 deletion to reveal the scope of RIDD in tumor DCs which may not recapitulate physiological responses, our work alludes to cDC1s as regulators of anti-melanoma T cell immunity in XBP1$^{\Delta DC}$ mice. First, cDC1s are the subset with the highest IRE1 RNase activity within melanoma and MC38 tumor niches, and T cell parameters altered by XBP1 loss in CD11c^{+} cells, such as the induction of intratumoral IFN-γ producing CD8^{+} T cells and the maintenance of precursor exhausted TCF1^{+}CD8^{+} T cells are attributed to cDC1 function (8, 11). Furthermore, these processes are also dependent on RIDD activation by DCs, which is more strongly induced in cDC1s from XBP1$^{\Delta DC}$ mice (25, 26). Nevertheless, as we also observe reduced frequencies of tumor infiltrating CD4^{+} IFNγ^{+} T cells in XBP1$^{\Delta DC}$ mice in melanoma and MC38 models, a contribution of IRE1 RNase in CD4^{+} T cell priming by tumor cDC1s (56) or also by cDC2s (17) cannot be excluded.

On a mechanistic level, we do not find a role for IRE1 RNase in cross-presentation of tumor antigens, contrasting with previous findings in steady state cDC1s (26). These data suggest that tumors may shape the spectra of XBP1s/RIDD targets in infiltrating cDC1s or that additional mechanisms (or DC subtypes) may compensate for the process. In fact, *tapbp* mRNA, a previously identified RIDD target in XBP1-deficient splenic DCs contributing to antigen cross-presentation is not found as DEG in the transcriptomic

analysis of this study. In addition, growing evidence demonstrating the capacity of tumor DCs to carry out cross-dressing of MHC-I/peptide complexes from tumor cells adds a new layer of complexity that remains to be addressed (57, 58). However, one novel candidate identified in this analysis as a potential RIDD substrate, the ER-resident FC receptor Like A (*Fcrla)* (Fig. 5A), has been previously identified as part of a BATF3/IRF8 transcriptional program that confers tumor immunogenicity in cDC1s independently of cross-presentation (59). As such, data presented here delineates for first time the XBP1s-dependent and RIDD-dependent targets in tumor cDC1s, which may serve as basis for future studies focused on addressing the role of selective IRE1 RNase targets involved in the regulation of antitumor immunity.

Multiple efforts are currently focused on the development of pharmacological compounds targeting the IRE1 RNase active site and XBP1s *in vivo*, many of which have shown translational potential in cancer (60). A recent study revealed that RIDD regulates expression of the MHC-I heavy chain mRNAs in DCs and that inhibition of IRE1 RNase through systemic administration of small molecules greatly attenuates tumor growth in 4T1 and CT26 models, by a mechanism proposed to be dependent on DC cross-presentation (61). Even though we do not find MHC-I heavy chain mRNAs as DEGs in the transcriptomic analysis of tumor cDC1s from XBP1$^{\Delta DC}$/IRE1^{trunc}DC mice, and we do not find an improved melanoma tumor response in XBP1$^{\Delta DC}$/IRE1^{trunc}DC animals, future studies are required to integrate these findings through experiments that include kinetics of comparable tumor models. Finally, the work presented here serves as a proof-of-concept study demonstrating that IRE1 RNase dependent, XBP1s-independent outputs in DCs may also contribute to fine-tuning antitumor immunity.

MATERIAL AND METHODS

RESOURCE AVAILABILITY

Further information and requests for resources and reagents should be directed to Fabiola Osorio (fabiolaosorio@med.uchile.cl).

Materials availability

This study did not generate new unique reagents.

Data and code availability

RNA-seq data have been deposited at GEO and are publicly available as of the date of publication. Accession numbers are listed in supplementary resources table. This paper does not report original code. Any additional information required to reanalyze the data reported in this paper is available upon request.

EXPERIMENTAL MODEL AND SUBJECT DETAILS

Mice

ERAI (33), XBP1^{WT}(XBP1fl/fl (36)), XBP1$^{\Delta DC}$ (XBP1fl/fl x CD11c-Cre (37)), XBP1^{WT}/IRE1^{WT} (XBP1fl/fl x IRE1fl/fl (45)), XBP1$^{\Delta DC}$ IRE1^{trunc}DC (XBP1fl/fl x IRE1fl/fl x CD11c-Cre) mice were bred at Universidad de Chile and Fundación Ciencia y Vida in specific pathogen-free conditions. Also, for RNA seq studies XBP1^{WT}, XBP1$^{\Delta DC}$, XBP1^{WT}/IRE1^{WT} and XBP1$^{\Delta DC}$ IRE1^{trunc}DC mice were bred at the animal facility at VIB institute. pmel-1 mice (40) were kindly donated by Dr F. Salazar-Onfray. All mice were kept on a C57BL/6 background. Litters with mice of both sexes at 6–14 weeks of age were used for experiments.

Cell Lines

B78-ChOVA cells were kindly provided by Dr. Matthew Krummel (UCSF) (2). B16-F10 cells were obtained from ATCG (#CRL-6475). B16-FLT3L cell line (62) was provided by Dr. Maria Rosa Bono (University of Chile). MC-38 cell line was provided by Dr. Álvaro Lladser (Universidad San Sebastian). Cells were cultured under standard conditions prior to injection into mice. Briefly, cells were cultured in DMEM (B78-ChOVA) or RPMI-1640 (B16-F10/B16-FLT3L/MC-38) supplemented with 10% v/v inactivated fetal bovine serum (FBS, Gibco), 100 U/mL penicillin (Corning), 100 µg/mL streptomycin (Corning) and 0.55 mM 2-Mercaptoethanol (Gibco). For MC-38 culture, media was supplemented additionally with non-essential amino acids (ThermoFisher Scientific) and 1 mM sodium pyruvate (ThermoFisher Scientific). Cells were cultured on T75 tissue-culture treated plastic flasks at 37°C, 5% CO_2. Cells were split every other day.

METHOD DETAILS

Tumor Model

Tumor cell lines were harvested, washed with PBS, and resuspended in a final injection volume of 50 µl PBS. $5x10^5$ (B16/B78-ChOVA) or $1x10^6$ (MC-38) tumor cells were injected in the right flank of shaved mice intradermally and allowed to grow for 10-15 days. For tumor growth curves, tumor size was determined by two orthogonal measurements with a caliper and the volume was estimated as (width^2 x length)/2.

Preparation of Cell Suspensions

Tumors were minced and digested with Collagenase D (1 mg/mL, Roche) and DNAse I (50 µg/mL, Roche) for 30 minutes at 37°C in a water bath. Digested tissue was then passed through a 70 µm cell strainer, followed by red blood cell lysis with RBC lysis buffer (Biolegend). Single cells were kept on ice.

For whole intratumoral immune cell profiling and DC stainings, CD45-biotin magnetic positive selection (MACS, Miltenyi) was performed to enrich for total tumor immune infiltrate.

For intratumoral T cell stainings, hematopoietic cells were enriched by density gradient centrifugation with 40/70 Percoll (GE Healthcare) for 20 min at 700xg.

Tumor draining lymph nodes (tdLNs) were minced and digested with Collagenase D (1 mg/mL, Roche) and DNAse I (50 µg/mL, Roche) for 45 minutes at 37°C in a water bath. Digested tissue was then passed through a 70 µm cell strainer and single cells were kept on ice.

Bone marrow derived DCs generation

Bone marrow cells from femurs and tibias were cultured in presence of 20 ng/ml mouse recombinant GM-CSF (Biolegend) for 8 days. Fresh culture medium with cytokine was added on day 3, and on day 6. After harvesting and when indicated, cells were stimulated with 1 ug/mL Tunicamycin (Sigma) for 8h followed by total RNA extraction with Trizol (Invitrogen).

Bone marrow derived cDC1s generation and tumor lysate stimulation

Bone marrow cells from femurs and tibias were cultured in presence of 100 ng/ml recombinant human FLT3-L (Peprotech). After three days of differentiation, cells were

plated onto a monolayer of OP9-DL1 stromal cells and co-cultured for additional 6 days as reported (38, 39).

For tumor lysate preparation B78-ChOVA cells were washed twice with PBS, resuspended at $8x10^6$ cells/mL in RPMI supplemented with 10% FBS and aliquoted in cryotubes. Cell suspensions were subjected to heat-shock (42°C for 60 min) followed by three cycles of freeze/thaw (liquid nitrogen/waterbath at 37°C). Tumor lysates were stored at -80°C until use.

BM-derived cDC1s were harvested and plated with B78-ChOVA lysates (50 uL/mL) in round-bottom p96 plates. After 14h, Brefeldin A (GolgiPlug, BD) was added and four hours later, cells were harvested and stained for intracellular IL-12p40 expression by flow cytometry.

Xbp1s splicing assay

Total RNA was isolated either by Trizol (Invitrogen) or RNAeasy plus Micro Kit (Qiagen). cDNA was prepared using M-MLV reverse transcriptase (Invitrogen). The following primers were used for conventional PCR amplification of total Xbp1: Fwd: 5'-ACACGCTTGGGAATGGACAC-3' and Rev: 5'-CCATGGGAAGATGTTCTGGG-3' (26); and for beta actin (*Actb*): Fwd: 5'-CTAAGGCCAACCGTGAAAAG-3' and Rev: 5'-TTGCTGATCCACATCTGCTG-3' or alternatively for beta actin (*Actb*): Fwd 5'-GTGACGTTGACATCCGTAAAGA-3' and Rev: 5'-GCCGGACTCATCGTACTCC-3'. PCR products were analyzed on agarose gels.

Flow Cytometry and Cell Sorting

For surface staining, cells were incubated with anti-Fc receptor antibody (anti-CD16/32, Biolegend) and then stained with fluorochrome-conjugated antibodies in FACS buffer (PBS + 1% FBS + 2mM EDTA) for 30 min at 4°C. Viability was assessed by staining with fixable viability Zombie (BioLegend) or LIVE/DEAD fixable (Invitrogen). A biotinylated antibody was used for F4/80 staining, followed by a second staining step with Streptoavidin-APC (Biolegend) for 30 min at 4°C. Flow cytometry was performed on BD Fortessa LSR instrument. Analysis of flow cytometry data was done using FlowJo software. Cell sorting was performed using a BD FACS Aria III.

Transcription Factors and Granzyme B intracellular staining

After surface staining, cells were fixed and permeabilized using Foxp3 transcription factor staining set (eBioscience) followed by intracellular staining of transcription factors (Foxp3, Tcf1, Tox) and/or granzyme B as indicated by the manufacturer protocol.

T cell stimulation and intracellular cytokine staining

Tumor and TdLN cell suspensions were stimulated *ex-vivo* prior to staining with 0.25 μM phorbol 12- myristate 13-acetate (PMA; Sigma) and 1 μg/mL Ionomycin (Sigma) at 37°C and 5% CO_2 for 3.5 hr in the presence of Brefeldin A (BD GolgiPlug). After stimulation, cells were surface stained as mentioned above. Then, cells were fixed and permeabilized using BD Cytofix/Cytoperm fixation/permeabilization kit (BD) followed by intracellular staining of cytokines (IFN-γ, IL-2 and TNF-α) as indicated by the manufacturer protocol.

Tetramer staining

652 For OVA-specific CD8+ T cell quantification cells were incubated with PE H2-K^{b}-OVA
653 (SIINFEKL) tetramers (MBL) at room temperature for 30 min protected from light,
654 followed by surface staining and FACS analysis.
655
656 ***t-SNE and clustering***
657 For tSNE visualization of tumor immune infiltrate a multicolor flow cytometry panel was
658 used including 19 parameters (FSC, SSC, Viability, CD45, VenusFP, XCR1, CD4, NK1.1,
659 CD26, F4/80, Ly6G, MHCII, CD24, CD3e, Ly6C, CD8a, CD11c, CD11b, CD19). Cells were
660 compensated for spillover between channels and pre-gated on CD45+ Live singlets using
661 FlowJo. Flowjo workspace was imported into the R environment using CytoML v2.4.0 ,
662 FlowWokspace v4.4.0 and FlowCore v2.4.0 packages (63–65). The intensity values of
663 marker expression were then biexp-transformed via the flowjo_biexp_trans function of
664 FlowWorkspace using parameters ChannelRange=4096, maxValue=262144, pos=4.5,
665 neg=0 and widthBasis=-10. Subsequently 5.000 cell events from each mouse (4 WT and 4
666 ERAI) were randomly sampled and combined for a total of 40.000 single cells. Sampled
667 data was min-max normalized, and subjected to dimensionality reduction by Barnes-
668 Hutts implementation of t-Distributed Stochastic Neighbor Embedding (tSNE) using
669 RtSNE v0.15 package (66). Thirteen parameters were used for tSNE construction (XCR1,
670 CD4, NK1.1, CD26, F4/80, Ly6G, MHCII, CD24, CD3e, Ly6C, CD8a, CD11c, CD11b and CD19)
671 and the parameters were set to iterations=1000 and perplexity =30. After dimensionality
672 reduction, automatic clustering was performed using density based spatial clustering
673 (DBSCAN) using DBSCAN v1.1.8 package (67). Dotplot for marker expression among
674 clusters and Violin plots for VenusFP were then generated using ggplot2 v3.3.5 package
675 (68).
676

677 ***In vivo T cell proliferation assay***

678 LN cells from pmel-1 TCR transgenic mice were isolated and enriched for CD8+ T cells by
679 magnetic negative selection using CD8+ T cell isolation kit (MACS, Miltenyi). Enriched
680 CD8+ T cells were surface stained and naïve CD8+ T cells were purified by cell sorting
681 (CD8a+, CD62L high, CD44low, CD25 neg). After sorting, naïve CD8+ T cells were labeled
682 with Cell Trace Violet (CTV, Invitrogen). $1x10^6$ naïve CD8+ T cells were adoptively
683 transferred into B16-F10 tumor-bearing mice at day 7 after tumor challenge. *In vivo*
684 proliferation and CD44/CD25 expression of transferred T cells was analyzed by FACS in
685 tumor draining lymph nodes 4 days after adoptive transfer.
686
687 ***RNA-seq***
688 Cell suspensions from tumor tissue pooled from 2-4 B16 bearing mice were enriched in
689 immune cells by positive selection with CD45+ biotin magnetic beads (MACS, Miltenyi).
690 Enriched cells were surface stained and 5-20 $x10^3$ intratumoral cDC1s were sorted
691 directly in RLT lysis buffer (Qiagen) containing 2-mercaptoethanol. Immediately after
692 sorting, collected cells were homogenized through vortex and frozen on dry ice before
693 storage at -80°C. Total RNA was extracted with RNAeasy Plus Micro kit (Qiagen). RNA
694 sequencing was performed at VIB Nucleomics Core using SMART-seq v4 pre-
695 amplification followed by single-end sequencing on Illumina NextSeq500. Preprocessing
696 of the RNA-seq data was performed by Trimmomatic v0.39 and quality control by FastQC
697 v0.11.8. Mapping to the reference mouse genome was performed by STAR v2.7.3a and
698 HTSeqCount v0.11.2 was used for counting. Limma v3.42.2 (69) was used to normalize
699 the data. Genes which did not meet the requirement of a count per million (cpm) value
700 larger than 1 in at least 4 samples were filtered. This resulted in an expression table
701 containing 11066 genes. EdgeR v3.28.0 (70) was utilized to perform differential

expression analysis. Benjamini-Hochberg correction was used to adjust the p-values for multiple testing. Differentially expressed genes were filtered as genes with a |FC| > 1.5 and adjusted p-value < 0.05. Heatmaps were created using pheatmap v1.0.12 package (71) on log2 normalized and mean centered gene expression data.

Gene Set Enrichment Analysis

Over-Representation Analysis (ORA) and Gene Set Enrichment Analysis (GSEA) were performed using *ClusterProfiler* v4.0.5 package (72) in R and Gene Ontology (GO) knowledgebase gene sets. ORA results were considered significant when the q-value was below 0.01. GSEA was performed on pre-ranked mode using as rank metric the signed log10 transformed p-values derived from the differential expression analysis. GSEA was run using the GO:BP database or literature lists of Xbp1-targets and RIDD-targets (47). Results were considered significant when the adjusted p-value was below 0.05.

QUANTIFICATION AND STATISTICAL ANALYSIS

No statistical methods were used to predetermine sample size. The experiments were not randomized, and the investigators were not blinded to allocation during experiments and outcome assessment. Statistical analysis was conducted using GraphPad Prism software (v9.1.2). Results are presented as mean ± SEM. Two groups were compared using two tailed t-test for normal distributed data (Shapiro-Wilk test) or using a non-parametric two-tailed Mann-Whitney test as indicated in figure legends. Multiple groups were compared using one-way ANOVA with Tukey post-test. A p-value < 0.05 was considered statistically significant.

STUDY APPROVAL

All animal procedures were performed in accordance with institutional guidelines for animal care of the Fundación Ciencia y Vida, the Faculty of Medicine, University of Chile and the VIB, Belgium, and were approved by the local ethics committee.

Author contributions

F.F, MR.B, S.J and F.O designed the research; F.F, S.R, S.G, C.F, D.F did the experiments. F.F, S.R, S.J and F.O analyzed the results; C.DN and C.M helped with RNA-seq data analysis; D.Fe provided technical assistance and experimental expertise, T.I and A.L provided critical reagents. F.F. and F.O wrote the manuscript

Acknowledgements

We thank Dr Laurie H. Glimcher (Dana-Farber Cancer Institute) for *Xbp1*$^{fl/fl}$ mice; Dr Matthew Krummel (UCSF) for the B78ChOVA cell line; the VIB nucleomics facility for doing the RNA seq experiments and facilities at Universidad de Chile and Fundación Ciencia & Vida. We thank members of the immunology and immunology and cellular stress laboratories for critical support.

This work was funded by an International Research Scholar grant from HHMI (HHMI#55008744, FO); FONDECYT grant No 1200793 (FO); FONDECYT grant No 1191438 (MR.B); CONICYT/FONDEQUIP/EQM140016; FONDECYT grant No 1212070 (AL); ANID grant FB210008 (MR.B and AL); CONICYT-PFCHA/DoctoradoNacional/2017-21170366 (F.F). The work in Belgium was funded by Stichting tegen Kanker (2014/283), FWO-EOS (ID 30837538) and ERC-CoG (ID 819314) (S.J.).

Declaration of interest

The authors declare no competing interests.

FIGURE LEGENDS

Figure 1. cDC1s are predominant cellular targets of IRE1 activation in melanoma tumors.

(A-F) B16-F10 melanoma cells were implanted intradermally on ERAI or control mice and 11 days after implantation, tumor tissue was analyzed by multicolor flow cytometry. n=4 mice per group, representative of two independent experiments. **(A)** t-SNE of 40.000 immune (CD45+) infiltrating cells from melanoma of ERAI or control mice. Colors indicate unsupervised clustering by DBSCAN. **(B)** Marker expression across the different cell clusters identified in (A). See also Supp. Fig 1A. **(C)** t-SNE map colored by VenusFP signal intensity from control or ERAI mice. cDC1 cluster is highlighted in a red circle. **(D)** VenusFP signal quantification across the different cell clusters identified in (A). Median fluorescence intensity for VenusFP is depicted with a "+" inside each violin plot. **(E-F)** Histograms (E) and quantification (F) of VenusFP signal from manually gated immune populations from B16-F10-bearing WT and ERAI mice (see gating strategy in Supp. Fig.2A). Statistical significance is depicted as compact letter display, ANOVA and Tukey post-test between ERAI mice. **(G-H)** Xbp1 splicing assay (G) of tumor cDC1s isolated by cell sorting from B16-FLT3L-bearing WT mice compared to BMDCs treated with 1 μg/mL of the ER-stressor Tunicamycin (Tun) or medium for 8h. (H) Bars show the image quantification of the ratio between Xbp1 spliced (Xbp1s) and total Xbp1 (Xbp1s + Xbp1u). n= 3 samples per group (representative of three independent experiments), mean ± s.e.m, ANOVA and Tukey post-test, ** $p<0.01$, *** $p<0.001$. **(I)** Quantification of VenusFP signal from tumor and tumor draining lymph node migratory (mig) and resident (res) cDCs (see gating strategy in Supp. Fig.2B). ** $p<0.01$, ANOVA and Tukey post-test between ERAI mice. n=4 mice per group, representative of two independent experiments, mean ± s.e.m. **(J)** Quantification of VenusFP signal from

795 intratumoral and spleen monocytes (CD11b^{hi} Ly6C^{hi} cells). *** p<0.001, t-test between
796 ERAI mice. n= 3 mice (ERAI) or 1 mouse (WT), representative of two independent
797 experiments, mean ± s.e.m.
798
799 **Figure 2. XBP1 deletion in CD11c-expressing cells results in increased melanoma**
800 **tumor growth**
801 XBP1^{WT} and XBP1$^{\Delta DC}$ mice were implanted with B78ChOVA tumors. **(A)** Tumor growth
802 curves monitored over a period of 12 days. n=19 mice per group. Pooled data from 4
803 independent experiments. **(B)** Tumor size at day 12 post implantation. * p<0.05, two-
804 tailed t-test. n= 51 mice (XBP1^{WT}) or 53 mice (XBP1$^{\Delta DC}$) from animals used throughout
805 this study (pooled data from 12 independent experiments), boxplot. **(C)** Cell counts for
806 tumor immune infiltrate (CD45+). n=31 mice (XBP1^{WT}) or 29 mice (XBP1$^{\Delta DC}$), pooled
807 data from 8 independent experiments, mean ± s.e.m. **(D)** Frequencies of intratumoral
808 cDC subsets. n=5-10, pooled data from two (cDC2) or three (cDC1) independent
809 experiments, mean ± s.e.m. (E) Frequencies of cDC subsets in TdLN. n=4 mice per group,
810 representative of two independent experiments, mean ± s.e.m. **(F-G)** Frequencies of
811 tumor lymphoid and myeloid populations. n=3-12 mice per group, pooled data from two
812 (neutrophils, TAMs, NK) or three (MdCs, T) independent experiments, mean ± s.e.m. **(H)**
813 Tumor Treg (CD3$^+$CD4$^+$Foxp3$^+$), Tconv (CD3$^+$CD4$^+$Foxp3$^-$) and CD8$^+$ T cells (CD3$^+$CD8$^+$)
814 frequencies. n=8 mice per group, pooled data from two independent experiments, mean
815 ± s.e.m.
816
817 **Figure 3. XBP1 deletion in CD11c-expressing cells results in impaired antitumor T**
818 **cell responses and dysbalanced precursor/terminal exhausted T cell ratio.**

(A) CD40 and PD-L1 expression by tumor cDCs from B78-ChOVA bearing $XBP1^{WT}$ or $XBP1^{\Delta DC}$ mice. n=7 mice per group, pooled data from two independent experiments, mean ± s.e.m. See also TdLN data in Supp. Fig 4A. **(B)** Intracellular IL-12 expression of *in vitro* generated cDC1s (FLT3-L/OP9-DL1) upon stimulation with B78-ChOVA lysates. Gated on cDC1s ($MHC\text{-}II^+$ $CD11c^+$ $CD8^+$ $CD11b^-$). *p < 0.05, two-tailed Mann-Whitney test. Each dot represents a biological replicate, n=5, data pooled from three independent experiments, mean ± s.e.m. **(C-D)** $Tetramer^+$ CD8+ T cell frequencies in tumor and TdLN from B78-ChOVA bearing $XBP1^{WT}$ or $XBP1^{\Delta DC}$ mice. Gated on $CD3^+CD8^+$ T cells. n=8 mice per group, pooled data from two independent experiments, mean ± s.e.m. **(E-G)** Cytokines expression by tumor $CD8^+$ T cells (E-F) or $CD4^+$ T cells (G) from B78-ChOVA bearing $XBP1^{WT}$ or $XBP1^{\Delta DC}$ mice after ex vivo stimulation with PMA/ION in the presence of BFA. *p < 0.05, two-tailed Mann-Whitney test. n=18 mice ($XBP1^{WT}$) or 17 mice ($XBP1^{\Delta DC}$), pooled data from 4 independent experiments, mean ± s.e.m. **(H-I)** Precursor exhausted ($PD1^+TCF1^+$ $TIM3^{neg}$) and terminal exhausted ($PD1^+TCF1^{neg}$ $TIM3^+$) $CD8^+$ T cell tumor frequencies from B78-ChOVA bearing $XBP1^{WT}$ or $XBP1^{\Delta DC}$ mice. Gated on $CD3^+CD8^+$ T cells. * p<0.05, **p<0.01, two-tailed t-test. N=8 mice per group, pooled data from two independent experiments, mean ± s.e.m.

Figure 4. Tumor cDC1s from XBP1ΔDC mice display signs of RIDD.

(A) Upon Cre mediated recombination in $XBP1^{fl/fl}$ mice, a premature stop codon is introduced in the *Xbp1* mRNA sequence, preventing the translation of a functional XBP1s protein. XBP1s absence is reported to trigger IRE1 RNase hyperactivation and induce RIDD in certain cell types (26, 36). However, IRE1 RNase activity can still be monitored by determining Xbp1 mRNA splicing ratio. (B) Scheme depicting LoxP sites and IRE1 splicing sites at *Xbp1* locus (top) and PCR analysis of Xbp1 splicing in intratumoral

cDC1s isolated from B16-bearing XBP1^{WT} and XBP1$^{\Delta DC}$ mice (bottom). Each lane represents different mice. Xbp1u: Xbp1 unspliced; Xbp1s: Xbp1 spliced; Actb: beta actin. (C) CD11c expression by intratumoral cDC1, cDC2 and TAMs from B16-bearing XBP1^{WT} and XBP1$^{\Delta DC}$ mice. Gray histogram depicts unstained control. * $p<0.05$, ** $p<0.01$, **** $p<0.0001$, two-tailed t-test. n=4 mice per group, representative of two independent experiments, mean ± s.e.m. (D) CD11c expression by cDC subsets in the TdLN from B16-bearing XBP1^{WT} and XBP1$^{\Delta DC}$ mice. Gray histogram depicts unstained control. *$p<0.05$, two-tailed Mann-Whitney test. n=4 mice per group, representative of two independent experiments, mean ± s.e.m.

Figure 5. Gene expression profiles of tumor cDC1s deficient for IRE1 RNase and XBP1.

WT, XBP1$^{\Delta DC}$ and XBP1$^{\Delta DC}$/IRE1^{trunc}DC mice were implanted with B16 tumors. After 12 days, tumor cDC1s were isolated by cell sorting and total RNA was sequenced by RNA-seq. **(A)** Heatmap of differentially expressed genes (DEGs). Three groups of genes were identified by the pattern of expression among the three genotypes. **(B)** Over representation analysis of DEGs over the Gene Ontology (GO) database. **(C)** Gene Set Enrichment Analysis (GSEA) of WT vs XBP1$^{\Delta DC}$ cDC1s using GO:Biological Process database. **(D)** GSEA of WT vs XBP1$^{\Delta DC}$/IRE1^{trunc}DC cDC1s using GO:Biological Process database. **(E-F)** GSEA using XBP1s- and RIDD-target gene sets from literature (So et al, 2012, Cell Metabolism).

Figure 6. RIDD activation in DCs accounts for the changes related to tumor growth and dysregulated antitumor T cell immunity noticed in XBP1ΔDC mice.

868 XBP1^{WT}/IRE1^{WT} and XBP1$^{\Delta DC}$/IRE1^{trunc}DC mice were implanted with B78ChOVA cells.
869 **(A)** Tumor growth curves monitored over a period of 12 days. n=20 mice
870 (XBP1^{WT}/IRE1^{WT}) or 24 mice (XBP1$^{\Delta DC}$/IRE1^{trunc}DC), data pooled from 4 independent
871 experiments. **(B)** Tumor size at day 12 post implantation. n=24 mice (XBP1^{WT}/IRE1^{WT})
872 or 28 mice (XBP1$^{\Delta DC}$/IRE1^{trunc}DC), data pooled from 5 independent experiments, mean ±
873 s.e.m. **(C-D)** Cytokines expression by tumor CD8^{+} T cells after ex vivo stimulation with
874 PMA/Ionomycin in the presence of BFA. Gated on CD3^{+}CD8^{+} T cells. N=9 mice
875 (XBP1^{WT}/IRE1^{WT}) or 11 mice (XBP1$^{\Delta DC}$/IRE1^{trunc}DC), data pooled from three
876 independent experiments, mean ± s.e.m. **(E-F)** Precursor exhausted (PD1^{+}TCF1^{+}
877 TIM3^{neg}) and terminal exhausted (PD1^{+}TCF1^{neg} TIM3^{+}) CD8^{+} T cell tumor frequencies.
878 Gated on CD3^{+}CD8^{+} T cells. n=9 mice (XBP1^{WT}/IRE1^{WT}) or 11 mice
879 (XBP1$^{\Delta DC}$/IRE1^{trunc}DC), data pooled from three independent experiments, mean ± s.e.m.
880

881 # SUPPLEMENTARY FIGURE LEGENDS

882 **Supplementary Figure 1. Immune analysis of melanoma tumors derived from**
883 **ERAI mice.**
884 **(A)** t-SNE map as in figure 1a. Color gradient shows the expression of the indicated
885 marker**. (B)** Quantification of VenusFP signal from manually gated immune populations
886 from MC-38 bearing WT and ERAI mice. **** $p < 0.0001$, ANOVA and Tukey post-test
887 between ERAI mice. n=3 (WT) or 5 (ERAI) mice per group, representative of two
888 independent experiments.(C) Quantification of VenusFP signal of tumor- and spleen-
889 cDC1s from MC-38 bearing WT and ERAI mice. **** $p<0.0001$, t-test between ERAI mice.
890 n=3 (WT) or 5 (ERAI), representative of two independent experiments.
891

Supplementary Figure 2. Gating strategy for tumor associated cDCs.

(A) Gating strategy for identification of immune infiltrated populations in tumors. Representative plots from B16 melanoma tumor. **(B)** Gating strategy for identification of migratory (mig) and resident (res) cDC1s and cDC2s in tumor draining lymph node. Representative plots from B16 melanoma TdLN.

Supplementary Figure 3. Tumor growth and T cell infiltration in MC-38 bearing XBP1$^{\Delta DC}$ mice.

XBP1^{WT} and XBP1$^{\Delta DC}$ mice were implanted with MC-38 tumors. **(A-C)** Tumor volume curves (A), tumor volumes (B) at end point and tumor weight (C) at end point. n=12-13 mice per group. Pooled data from two independent experiments.

Supplementary Figure 4. Tumor immune cell analysis of XBP1$^{\Delta DC}$ mice.

(A) Related to figure 3A. CD40 and PD-L1 expression by TdLN cDCs**.** n=7 mice per group, pooled data from two independent experiments, mean ± s.e.m. **(B)** Related to figure 3B. Dot plots of IL-12 intracellular expression by *in vitro* generated cDC1s stimulated with B78-ChOVA lysates**. (C)** Related to figure 3C-D. Fluorescence minus one (FMO) and tumor-free WT mouse as negative controls for tetramer staining. **(D-E)** XBP1^{WT} and XBP1$^{\Delta DC}$ mice were implanted with B16-F10 tumors. Seven days after implantation, CD8^{+} naïve T cells isolated from pmel1 transgenic mice were labeled with Cell Trace Violet and were adoptively transferred into tumor-bearing mice. Four days later, transferred cell proliferation and CD44/CD25 expression was quantified by FACS. n=8 mice (XBP1^{WT}) or 15 mice (XBP1$^{\Delta DC}$), data pooled from two independent experiments, mean ± s.e.m. **(F-G)** CD8+ T cell (F) and CD4+ T cell (G) frequencies and profiles in MC-38 bearing XBP1^{WT} and XBP1$^{\Delta DC}$ mice. n=11-13, pooled data from two independent

experiments, mean ± s.e.m. **(H)** Related to figure 3H-I. Representative histograms of different markers associated with terminal exhausted $CD8^+$ T cells. Gated on $CD3^+CD8^+PD1^+TCF1^+$ or $CD3^+CD8^+PD1^+TIM3^+$ as shown in figure 3H.

Supplementary Figure 5. IRE1/XBP1s double deficient cDC1s are unable to activate RIDD.

(A) PCR analysis of Xbp1 splicing in intratumoral cDC1s isolated from B16-bearing $XBP1^{WT}/IRE1^{WT}$ vs $XBP1^{\Delta DC}/IRE1^{trunc}$DC mice. Each lane represents different mice. Xbp1u: Xbp1 unspliced; Xbp1s: Xbp1 spliced; Actb: beta actin. **(B)** CD11c expression by intratumoral cDC1, cDC2 and TAMs from B16-bearing $XBP1^{WT}/IRE1^{WT}$ vs $XBP1^{\Delta DC}/IRE1^{trunc}$DC mice. n=4 mice per group, mean ± s.e.m. **(C)** CD11c expression by cDC subsets in the TdLN from B16-bearing $XBP1^{WT}/IRE1^{WT}$ vs $XBP1^{\Delta DC}/IRE1^{trunc}$DC mice. *p<0.05, two-tailed Mann-Whitney test. n=4 mice per group, mean ± s.e.m.

Supplementary Figure 6. RNAseq analysis of WT, XBP1 deficient WT vs IRE1/XBP1 double deficient cDC1s.

(A) Heatmap of genes with an adjusted p-value < 0.05 but with a fold change (FC) below the 1.5 threshold. Table summarize log2FC and adj p-values for WT vs XBP1 and WT vs IRE1/XBP1 deficient cDC1s. **(B)** Related to figure 5F-G. GSEA using XBP1s- and RIDD-target gene sets from literature (So et al, 2012, Cell Metabolism). **(C)** GSEA of the "triglyceride biosynthetic process" gene set (GO: 0019432) in WT vs $XBP1^{\Delta DC}$ cDC1s (left) or WT vs $XBP1^{\Delta DC}/IRE1^{trunc}$DC cDC1s (right) showing not statistically significant enrichment (q-value > 0.05). **(D)** Normalized expression (z-scores) for genes of the "triglyceride biosynthetic process" gene set (GO: 0019432) in WT, $XBP1^{\Delta DC}$, or $XBP1^{\Delta DC}/IRE1^{trunc}$DC cDC1s.

REFERENCES

1. Hildner K et al. Batf3 Deficiency Reveals a Critical Role for CD8 + Dendritic Cells in Cytotoxic T Cell Immunity. *Science* 2008;322(5904):1097–1100.

2. Broz ML et al. Dissecting the Tumor Myeloid Compartment Reveals Rare Activating Antigen-Presenting Cells Critical for T Cell Immunity. *Cancer Cell* 2014;26(5):638–652.

3. Roberts EW et al. Critical Role for CD103+/CD141+ Dendritic Cells Bearing CCR7 for Tumor Antigen Trafficking and Priming of T Cell Immunity in Melanoma. *Cancer Cell* 2016;30(2):324–336.

4. Spranger S, Dai D, Horton B, Gajewski TF. Tumor-Residing Batf3 Dendritic Cells Are Required for Effector T Cell Trafficking and Adoptive T Cell Therapy. *Cancer Cell* 2017;31(5):711-723.e4.

5. Böttcher JP et al. NK Cells Stimulate Recruitment of cDC1 into the Tumor Microenvironment Promoting Cancer Immune Control. *Cell* 2018;172(5):1022-1028.e14.

6. Chow MT et al. Intratumoral Activity of the CXCR3 Chemokine System Is Required for the Efficacy of Anti-PD-1 Therapy. *Immunity* 2019;50(6):1498-1512.e5.

7. Gerhard GM, Bill R, Messemaker M, Klein AM, Pittet MJ. Tumor-infiltrating dendritic cell states are conserved across solid human cancers. *J. Exp. Med.* 2021;218(1):e20200264.

8. Schenkel JM et al. Conventional type I dendritic cells maintain a reservoir of proliferative tumor-antigen specific TCF-1+ CD8+ T cells in tumor-draining lymph nodes. *Immunity* 2021;54(10):2338-2353.e6.

9. Barry KC et al. A natural killer–dendritic cell axis defines checkpoint therapy–responsive tumor microenvironments. *Nat. Med.* 2018;24(8):1178–1191.

10. Sánchez-Paulete AR et al. Cancer immunotherapy with immunomodulatory anti-CD137 and anti–PD-1 monoclonal antibodies requires BATF3-dependent dendritic cells. *Cancer Discov.* 2016;6(1):71–79.

11. Salmon H et al. Expansion and Activation of CD103+ Dendritic Cell Progenitors at the Tumor Site Enhances Tumor Responses to Therapeutic PD-L1 and BRAF Inhibition. *Immunity* 2016;44(4):924–938.

12. Garris CS et al. Successful Anti-PD-1 Cancer Immunotherapy Requires T Cell-Dendritic Cell Crosstalk Involving the Cytokines IFN-γ and IL-12. *Immunity* 2018;49(6):1148-1161.e7.

13. Hammerich L et al. Systemic clinical tumor regressions and potentiation of PD1 blockade with in situ vaccination. *Nat. Med.* 2019;25(5):814–824.

14. Oba T et al. Overcoming primary and acquired resistance to anti-PD-L1 therapy by induction and activation of tumor-residing cDC1s. *Nat. Commun.* 2020;11(1). doi:10.1038/s41467-020-19192-z

15. Maier B et al. A conserved dendritic-cell regulatory program limits antitumour immunity. *Nature* 2020;580:256–262.

16. Di Pilato M et al. CXCR6 positions cytotoxic T cells to receive critical survival signals in the tumor microenvironment. *Cell* 2021;184(17):4512-4530.e22.

17. Binnewies M et al. Unleashing Type-2 Dendritic Cells to Drive Article Unleashing Type-2 Dendritic Cells to Drive Protective Antitumor CD4 + T Cell Immunity. *Cell* 2019;177:1–16.

18. Walter P, Ron D. The unfolded protein response: From stress pathway to homeostatic regulation. *Science (80-.).* 2011;334(6059):1081–1086.

19. Yoshida H, Matsui T, Yamamoto A, Okada T, Mori K. XBP1 mRNA Is Induced by ATF6 and Spliced by IRE1 in Response to ER Stress to Produce a Highly Active Transcription Factor2001;107:881–891.

20. Calfon M et al. IRE1 couples endoplasmic reticulum load to secretory capacity by processing the XBP-1 mRNA2002;415(January):1–6.

21. Hollien J et al. Regulated Ire1-dependent decay of messenger RNAs in mammalian cells. *J. Cell Biol.* 2009;186(3):323–331.

22. Maurel M, Chevet E, Tavernier J, Gerlo S. Getting RIDD of RNA: IRE1 in cell fate regulation. *Trends Biochem. Sci.* 2014;39(5):245–254.

23. Wang JM et al. IRE1 prevents hepatic steatosis by processing and promoting the degradation of select microRNAs. *Sci. Signal.* 2018;11(530):eaao4617.

24. Fink SL et al. IRE1a promotes viral infection by conferring resistance to apoptosis. *Sci. Signal.* 2017;10(482):eaai7814.

25. Tavernier SJ et al. Regulated IRE1-dependent mRNA decay sets the threshold for dendritic cell survival. *Nat. Cell Biol.* 2017;19(6):698–710.

26. Osorio F et al. The unfolded-protein-response sensor IRE-1α regulates the function of CD8α+ dendritic cells. *Nat. Immunol.* 2014;15(3):248–257.

27. Chen X, Cubillos-Ruiz JR. Endoplasmic reticulum stress signals in the tumour and its microenvironment. *Nat. Rev. Cancer* 2020;21(February):71–88.

28. Song M, Cubillos-ruiz JR. Endoplasmic Reticulum Stress Responses in Intratumoral Immune Cells : Implications for Cancer Immunotherapy. *Trends Immunol.* 2019;40(2):128–141.

29. Guilliams M et al. Unsupervised High-Dimensional Analysis Aligns Dendritic Cells across Tissues and Species. *Immunity* 2016;45(3):669–684.

30. Cubillos-Ruiz JR et al. ER Stress Sensor XBP1 Controls Anti-tumor Immunity by Disrupting Dendritic Cell Homeostasis. *Cell* 2015;161(7):1527–1538.

31. Dong H et al. The IRE1 endoplasmic reticulum stress sensor activates natural killer cell immunity in part by regulating c-Myc. *Nat. Immunol.* 2019;20(7):865–878.

32. Song M et al. IRE1α–XBP1 controls T cell function in ovarian cancer by regulating mitochondrial activity. *Nature* 2018;562(7727):423–428.

33. Iwawaki T, Akai R, Kohno K, Miura M. A transgenic mouse model for monitoring endoplasmic reticulum stress. *Nat. Med.* 2004;10(1):98–102.

34. Mach N et al. Differences in dendritic cells stimulated in vivo by tumors engineered to secrete granulocyte-macrophage colony-stimulating factor or Flt3-ligand. *Cancer Res.* 2000;60(12):3239–3246.

35. Ruhland MK et al. Visualizing Synaptic Transfer of Tumor Antigens among Dendritic Cells. *Cancer Cell* 2020;37(6):786-799.e5.

1026 36. Lee A, Scapa E, Cohen D, Glimcher L. Regulation of hepatic lipogenesis by the
1027 transcription factor XBP1. *Science* 2008;320(5882):1492–1496.

1028 37. Caton ML, Smith-Raska MR, Reizis B. Notch–RBP-J signaling controls the homeostasis
1029 of CD8 ⁻ dendritic cells in the spleen. *J. Exp. Med.* 2007;204(7):1653–1664.

1030 38. Cells CCD et al. Notch Signaling Facilitates In Vitro Generation of Resource Notch
1031 Signaling Facilitates In Vitro Generation of Cross-Presenting Classical Dendritic
1032 Cells2018;3658–3672.

1033 39. Balan S et al. Large-Scale Human Dendritic Cell Differentiation Revealing Notch-
1034 Dependent Lineage Bifurcation and Heterogeneity. *Cell Rep.* 2018;24(7):1902-1915.e6.

1035 40. Overwijk WW et al. Tumor Regression and Autoimmunity after Reversal of a
1036 Functionally Tolerant State of Self-reactive CD8 ⁺ T Cells. *J. Exp. Med.* 2003;198(4):569–
1037 580.

1038 41. Miller BC et al. Subsets of exhausted CD8+ T cells differentially mediate tumor
1039 control and respond to checkpoint blockade. *Nat. Immunol.* 2019;20(3):326–336.

1040 42. Philip M, Schietinger A. CD8+ T cell differentiation and dysfunction in cancer. *Nat.*
1041 *Rev. Immunol.* 2021;Online ahead of print.

1042 43. Chen Z et al. TCF-1-Centered Transcriptional Network Drives an Effector versus
1043 Exhausted CD8 T Cell-Fate Decision. *Immunity* 2019;51(5):840-855.e5.

1044 44. Sade-Feldman M et al. Defining T Cell States Associated with Response to Checkpoint
1045 Immunotherapy in Melanoma. *Cell* 2018;175(4):998-1013.e20.

1046 45. Iwawaki T, Akai R, Yamanaka S, Kohno K. Function of IRE1 alpha in the placenta is
1047 essential for placental development and embryonic viability. *Proc. Natl. Acad. Sci. U. S. A.*
1048 2009;106(39):16657–16662.

1049 46. Lee AS. The ER chaperone and signaling regulator GRP78/BiP as a monitor of
1050 endoplasmic reticulum stress. *Methods* 2005;35(4):373–381.

1051 47. So JS et al. Silencing of lipid metabolism genes through ire1α-mediated Mrna decay
1052 lowers plasma lipids in mice. *Cell Metab.* 2012;16(4):487–499.

1053 48. Janssens S, Pulendran B, Lambrecht BN. Emerging functions of the unfolded protein
1054 response in immunity. *Nat. Immunol.* 2014;15(10):910–919.

1055 49. Grootjans J, Kaser A, Kaufman RJ, Blumberg RS. The unfolded protein response in
1056 immunity and inflammation. *Nat. Rev. Immunol.* 2016;16(8):469–484.

1057 50. Shaffer AL et al. XBP1, downstream of Blimp-1, expands the secretory apparatus and
1058 other organelles, and increases protein synthesis in plasma cell differentiation.
1059 *Immunity* 2004;21(1):81–93.

1060 51. Bettigole SE et al. The transcription factor XBP1 is selectively required for eosinophil
1061 differentiation. *Nat. Immunol.* 2015;16(8):829–837.

1062 52. Batista A et al. IRE1α regulates macrophage polarization, PD-L1 expression, and
1063 tumor survival. *PLoS Biol.* 2020;18(6):1–26.

1064 53. Scarlett UK et al. Ovarian cancer progression is controlled by phenotypic changes in
1065 dendritic cells. *J. Exp. Med.* 2012;209(3):495–506.

1066 54. Huarte E et al. Depletion of dendritic cells delays ovarian cancer progression by
1067 boosting antitumor immunity. *Cancer Res.* 2008;68(18):7684–7691.

55. Fuertes MB et al. Host type I IFN signals are required for antitumor CD8 + T cell responses through CD8α + dendritic cells. *J. Exp. Med.* 2011;208(10):2005–2016.

56. Ferris ST et al. cDC1 prime and are licensed by CD4+ T cells to induce anti-tumour immunity. *Nature* 2020;584(7822):624–629.

57. Duong E et al. Type I interferon activates MHC class I-dressed CD11b+ conventional dendritic cells to promote protective anti-tumor CD8+ T cell immunity. *Immunity* 2022;55(2):308-323.e9.

58. MacNabb BW et al. Dendritic cells can prime anti-tumor CD8+ T cell responses through major histocompatibility complex cross-dressing. *Immunity* 2022;55(6):982-997.e8.

59. Theisen DJ et al. Batf3-dependent genes control tumor rejection induced by dendritic cells independently of cross-presentation. *Cancer Immunol. Res.* 2019;7(1):29–39.

60. Marciniak SJ, Chambers JE, Ron D. Pharmacological targeting of endoplasmic reticulum stress in disease. *Nat. Rev. Drug Discov.* 2022;21(2):115–140.

61. Guttman O et al. Antigen-derived peptides engage the ER stress sensor IRE1α to curb dendritic cell cross-presentation. *J. Cell Biol.* 2022;221(6). doi:10.1083/jcb.202111068

62. Guo-Ping S et al. Cathepsin S required for normal MHC class II peptide loading and germinal center development. *Immunity* 1999;10(2):197–206.

63. Finak G, Jiang W, Gottardo R. CytoML for cross-platform cytometry data sharing. *Cytom. Part A* 2018;93(12):1189–1196.

64. Ellis B et al. flowCore: flowCore: Basic structures for flow cytometry data2021;

65. Finak G, Jiang M. flowWorkspace: Infrastructure for representing and interacting with gated and ungated cytometry data sets2021;

66. Krijthe JH. Rtsne: T-Distributed Stochastic Neighbor Embedding using a Barnes-Hut Implementation2015;

67. Hahsler M, Piekenbrock M, Doran D. Dbscan: Fast density-based clustering with R. *J. Stat. Softw.* 2019;91(1). doi:10.18637/jss.v091.i01

68. Wickham H. *ggplot2: Elegant Graphics for Data Analysis*. Springer-Verlag New York; 2016:

69. Ritchie ME et al. Limma powers differential expression analyses for RNA-sequencing and microarray studies. *Nucleic Acids Res.* 2015;43(7):e47.

70. Robinson M, McCarthy D, Smyth G. edgeR: a Bioconductor package for differential expression analysis of digital gene expression data. *Bioinformatics* 2010;26:139–140.

71. Kolde R. pheatmap: Pretty Heatmaps2019;

72. Wu T et al. clusterProfiler 4.0: A universal enrichment tool for interpreting omics data. *Innov.* 2021;2(3):100141.

Figure 1

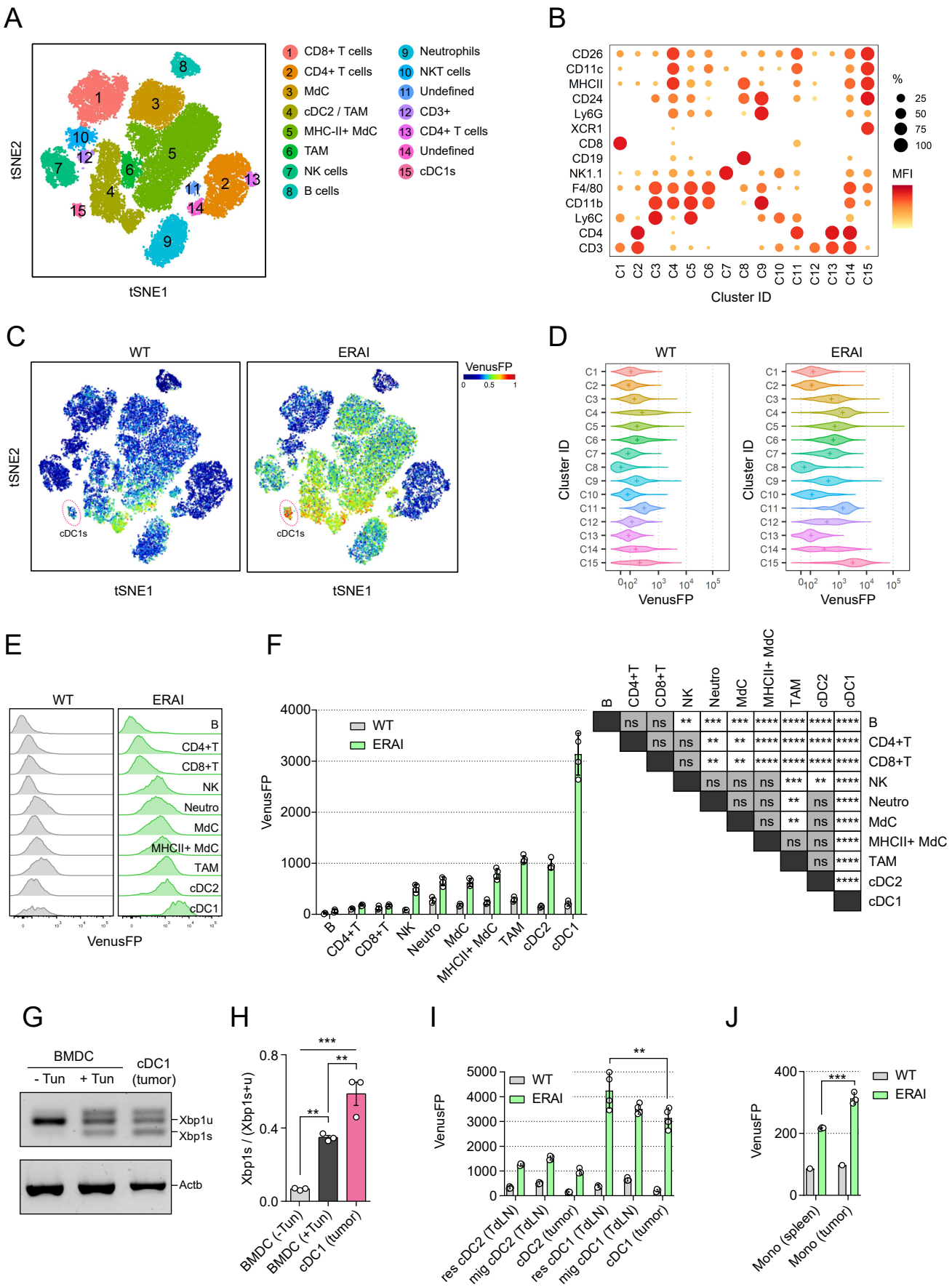
A
tSNE2
tSNE1
1 CD8+ T cells
2 CD4+ T cells
3 MdC
4 cDC2 / TAM
5 MHC-II+ MdC
6 TAM
7 NK cells
8 B cells
9 Neutrophils
10 NKT cells
11 Undefined
12 CD3+
13 CD4+ T cells
14 Undefined
15 cDC1s
B
CD26
CD11c
MHCII
CD24
Ly6G
XCR1
CD8
CD19
NK1.1
F4/80
CD11b
Ly6C
CD4
CD3
%
25
50
75
100
MFI
C1 C2 C3 C4 C5 C6 C7 C8 C9 C10 C11 C12 C13 C14 C15
Cluster ID
C
WT
ERAI
VenusFP
0 0.5 1
cDC1s
tSNE1
D
WT
ERAI
Cluster ID
VenusFP
E
WT
ERAI
B
CD4+T
CD8+T
NK
Neutro
MdC
MHCII+ MdC
TAM
cDC2
cDC1
VenusFP
F
WT
ERAI
VenusFP
4000
3000
2000
1000
0
B CD4+T CD8+T NK Neutro MdC MHCII+ MdC TAM cDC2 cDC1
ns ** *** **** ns
G
BMDC
- Tun + Tun
cDC1 (tumor)
Xbp1u
Xbp1s
Actb
H
Xbp1s / (Xbp1s+u)
0.8
0.4
0.0
BMDC (-Tun)
BMDC (+Tun)
cDC1 (tumor)
I
WT
ERAI
VenusFP
5000
4000
3000
2000
1000
0
res cDC2 (TdLN)
mig cDC2 (TdLN)
cDC2 (tumor)
res cDC1 (TdLN)
mig cDC1 (TdLN)
cDC1 (tumor)
J
WT
ERAI
VenusFP
400
200
0
Mono (spleen)
Mono (tumor)

Figure 2

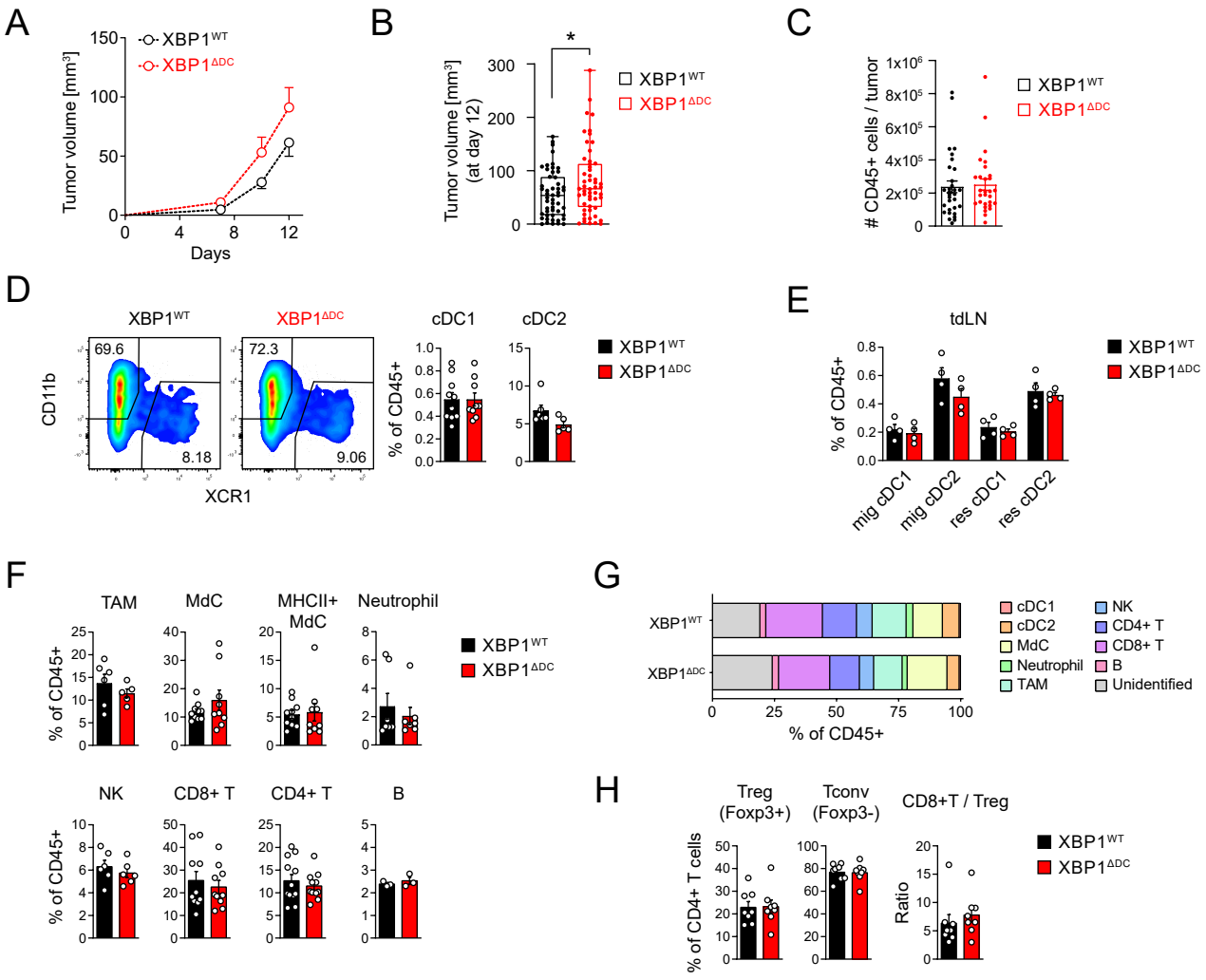
A
Tumor volume [mm3]
Days
XBP1WT
XBP1ΔDC
B
Tumor volume [mm3] (at day 12)
*
C
CD45+ cells / tumor
D
CD11b
XCR1
69.6
8.18
72.3
9.06
% of CD45+
cDC1
cDC2
E
tdLN
mig cDC1
mig cDC2
res cDC1
res cDC2
F
TAM
MdC
MHCII+ MdC
Neutrophil
NK
CD8+ T
CD4+ T
B
G
% of CD45+
cDC1
cDC2
MdC
Neutrophil
TAM
NK
CD4+ T
CD8+ T
B
Unidentified
H
Treg (Foxp3+)
Tconv (Foxp3-)
CD8+T / Treg
% of CD4+ T cells
Ratio

Figure 3

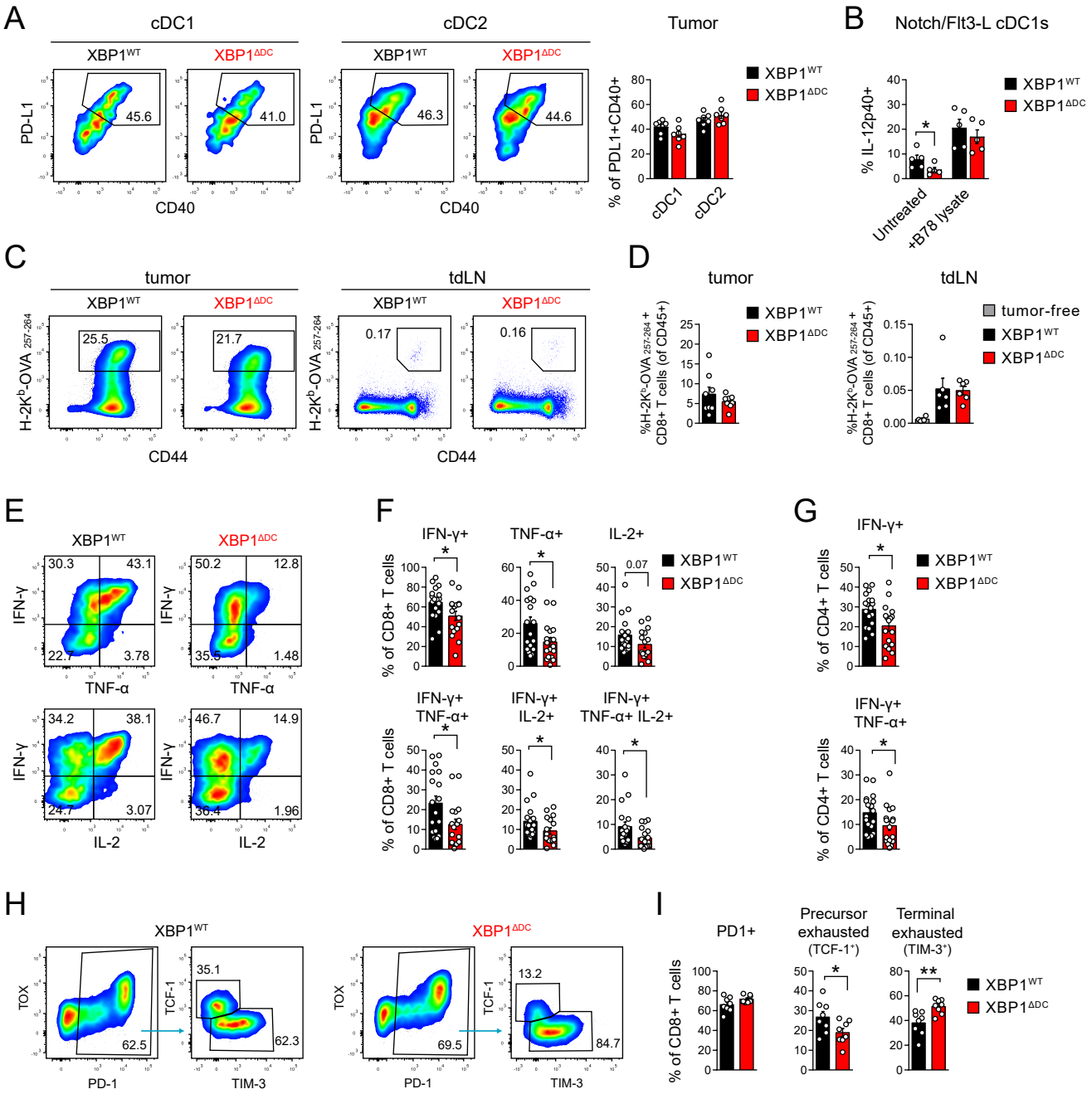
A
cDC1
cDC2
Tumor
XBP1WT
XBP1ΔDC
PD-L1
CD40
45.6
41.0
46.3
44.6
% of PDL1+CD40+
cDC1
cDC2
B
Notch/Flt3-L cDC1s
% IL-12p40+
Untreated
+B78 lysate
C
tumor
tdLN
H-2Kb-OVA 257-264
CD44
25.5
21.7
0.17
0.16
D
%H-2Kb-OVA 257-264 + CD8+ T cells (of CD45+)
tumor-free
E
IFN-γ
TNF-α
IL-2
30.3
43.1
22.7
3.78
50.2
12.8
35.5
1.48
34.2
38.1
24.7
3.07
46.7
14.9
36.4
1.96
F
IFN-γ+
TNF-α+
IL-2+
IFN-γ+ TNF-α+
IFN-γ+ IL-2+
IFN-γ+ TNF-α+ IL-2+
% of CD8+ T cells
0.07
G
% of CD4+ T cells
H
TOX
TCF-1
PD-1
TIM-3
35.1
62.5
62.3
13.2
69.5
84.7
I
PD1+
Precursor exhausted (TCF-1+)
Terminal exhausted (TIM-3+)

Figure 4

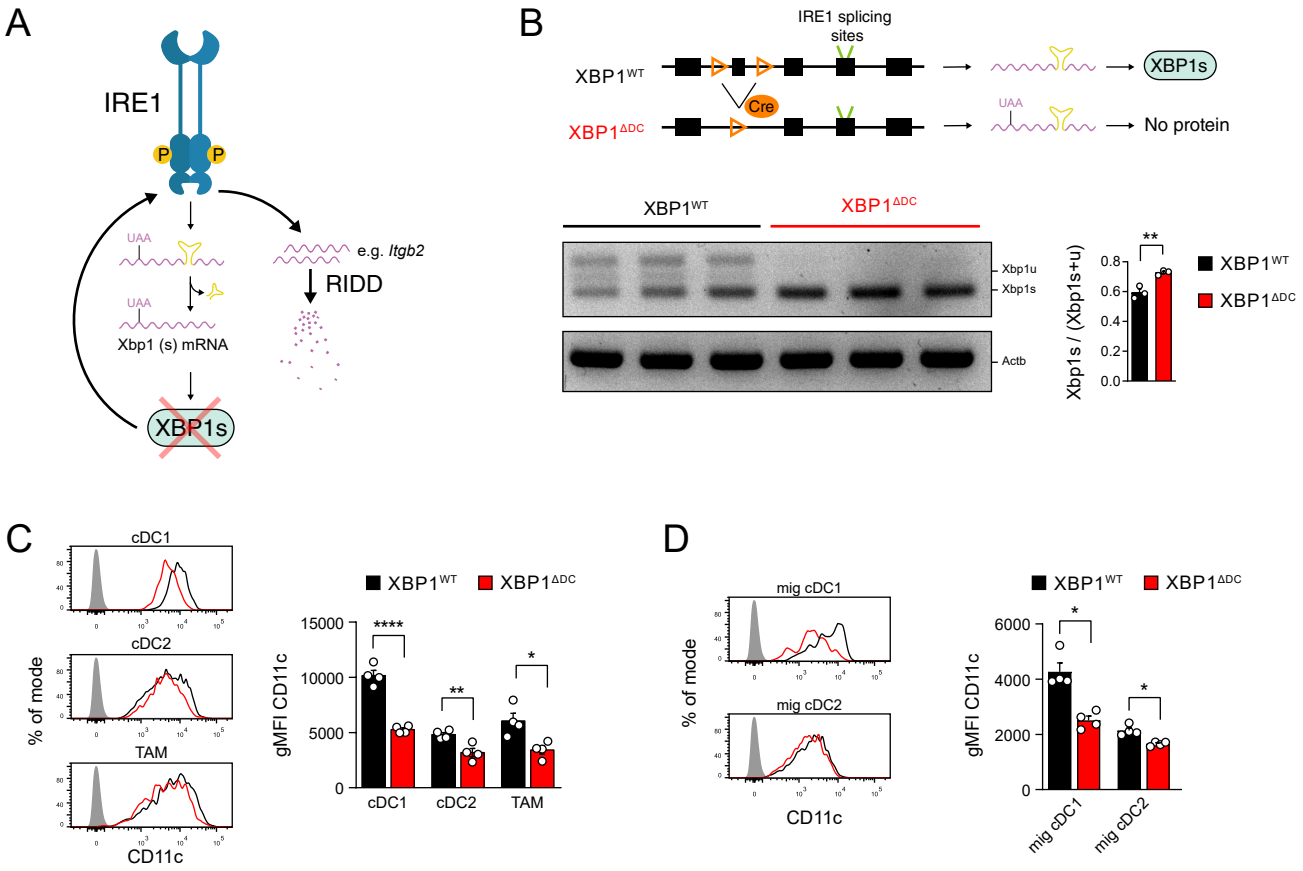
A
IRE1
P
P
UAA
UAA
Xbp1 (s) mRNA
e.g. Itgb2
RIDD
XBP1s
B
IRE1 splicing sites
XBP1WT
Cre
XBP1ΔDC
XBP1s
UAA
No protein
XBP1WT
XBP1ΔDC
Xbp1u
Xbp1s
Actb
Xbp1s / (Xbp1s+u)
0.8
0.6
0.4
0.2
0.0
**
XBP1WT
XBP1ΔDC
C
cDC1
cDC2
TAM
% of mode
CD11c
XBP1WT
XBP1ΔDC
gMFI CD11c
15000
10000
5000
0
****
**
*
cDC1
cDC2
TAM
D
mig cDC1
mig cDC2
% of mode
CD11c
XBP1WT
XBP1ΔDC
gMFI CD11c
6000
4000
2000
0
*
*
mig cDC1
mig cDC2

Figure 5

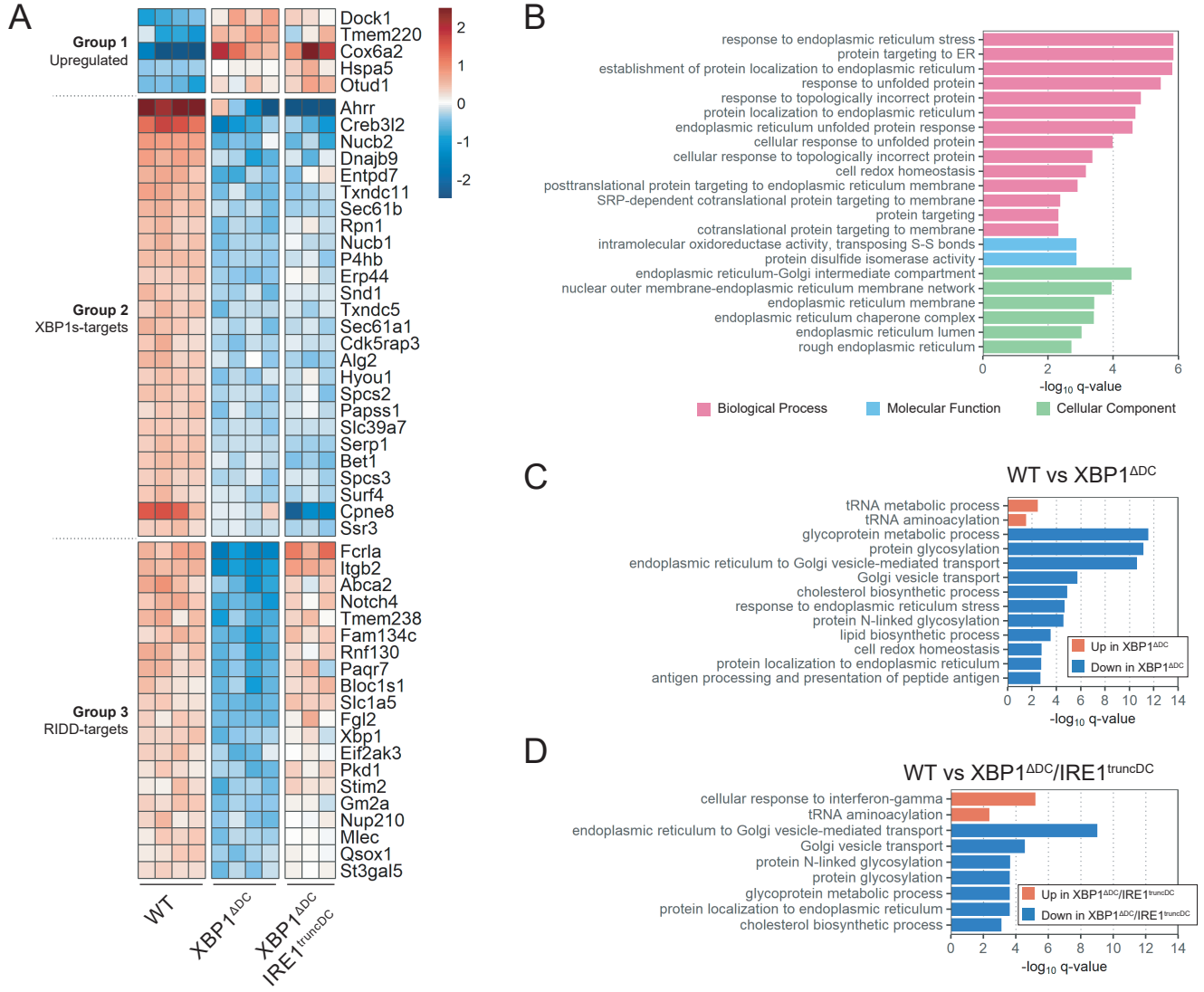
A
Group 1
Upregulated
Group 2
XBP1s-targets
Group 3
RIDD-targets
Dock1
Tmem220
Cox6a2
Hspa5
Otud1
Ahrr
Creb3l2
Nucb2
Dnajb9
Entpd7
Txndc11
Sec61b
Rpn1
Nucb1
P4hb
Erp44
Snd1
Txndc5
Sec61a1
Cdk5rap3
Alg2
Hyou1
Spcs2
Papss1
Slc39a7
Serp1
Bet1
Spcs3
Surf4
Cpne8
Ssr3
Fcrla
Itgb2
Abca2
Notch4
Tmem238
Fam134c
Rnf130
Paqr7
Bloc1s1
Slc1a5
Fgl2
Xbp1
Eif2ak3
Pkd1
Stim2
Gm2a
Nup210
Mlec
Qsox1
St3gal5
2
1
0
-1
-2
WT
XBP1ΔDC
XBP1ΔDC IRE1truncDC
B
response to endoplasmic reticulum stress
protein targeting to ER
establishment of protein localization to endoplasmic reticulum
response to unfolded protein
response to topologically incorrect protein
protein localization to endoplasmic reticulum
endoplasmic reticulum unfolded protein response
cellular response to unfolded protein
cellular response to topologically incorrect protein
cell redox homeostasis
posttranslational protein targeting to endoplasmic reticulum membrane
SRP-dependent cotranslational protein targeting to membrane
protein targeting
cotranslational protein targeting to membrane
intramolecular oxidoreductase activity, transposing S-S bonds
protein disulfide isomerase activity
endoplasmic reticulum-Golgi intermediate compartment
nuclear outer membrane-endoplasmic reticulum membrane network
endoplasmic reticulum membrane
endoplasmic reticulum chaperone complex
endoplasmic reticulum lumen
rough endoplasmic reticulum
0 2 4 6
-log10 q-value
Biological Process
Molecular Function
Cellular Component
C
WT vs XBP1ΔDC
tRNA metabolic process
tRNA aminoacylation
glycoprotein metabolic process
protein glycosylation
endoplasmic reticulum to Golgi vesicle-mediated transport
Golgi vesicle transport
cholesterol biosynthetic process
response to endoplasmic reticulum stress
protein N-linked glycosylation
lipid biosynthetic process
cell redox homeostasis
protein localization to endoplasmic reticulum
antigen processing and presentation of peptide antigen
Up in XBP1ΔDC
Down in XBP1ΔDC
0 2 4 6 8 10 12 14
-log10 q-value
D
WT vs XBP1ΔDC/IRE1truncDC
cellular response to interferon-gamma
tRNA aminoacylation
endoplasmic reticulum to Golgi vesicle-mediated transport
Golgi vesicle transport
protein N-linked glycosylation
protein glycosylation
glycoprotein metabolic process
protein localization to endoplasmic reticulum
cholesterol biosynthetic process
Up in XBP1ΔDC/IRE1truncDC
Down in XBP1ΔDC/IRE1truncDC
0 2 4 6 8 10 12 14
-log10 q-value
E
WT vs XBP1ΔDC
XBP1s-targets
Running ES
0.00
-0.25
-0.50
-0.75
NES = -2.8
q-value = 9.0E-26
Rank in Gene List
RIDD-targets
0.0
-0.2
-0.4
-0.6
-0.8
NES = -2.8
q-value = 1.6E-22
Rank in Gene List
Up
XBP1ΔDC
Up
WT
F
WT vs XBP1ΔDC/IRE1truncDC
XBP1s-targets
Running ES
0.00
-0.25
-0.50
-0.75
NES = -2.9
q-value = 3.4E-22
Rank in Gene List
RIDD-targets
0.1
0.0
-0.1
-0.2
-0.3
-0.4
NES = -1.6
q-value = 3.8E-3
Rank in Gene List
Up
XBP1ΔDC/IRE1truncDC
Up
WT

Figure 6

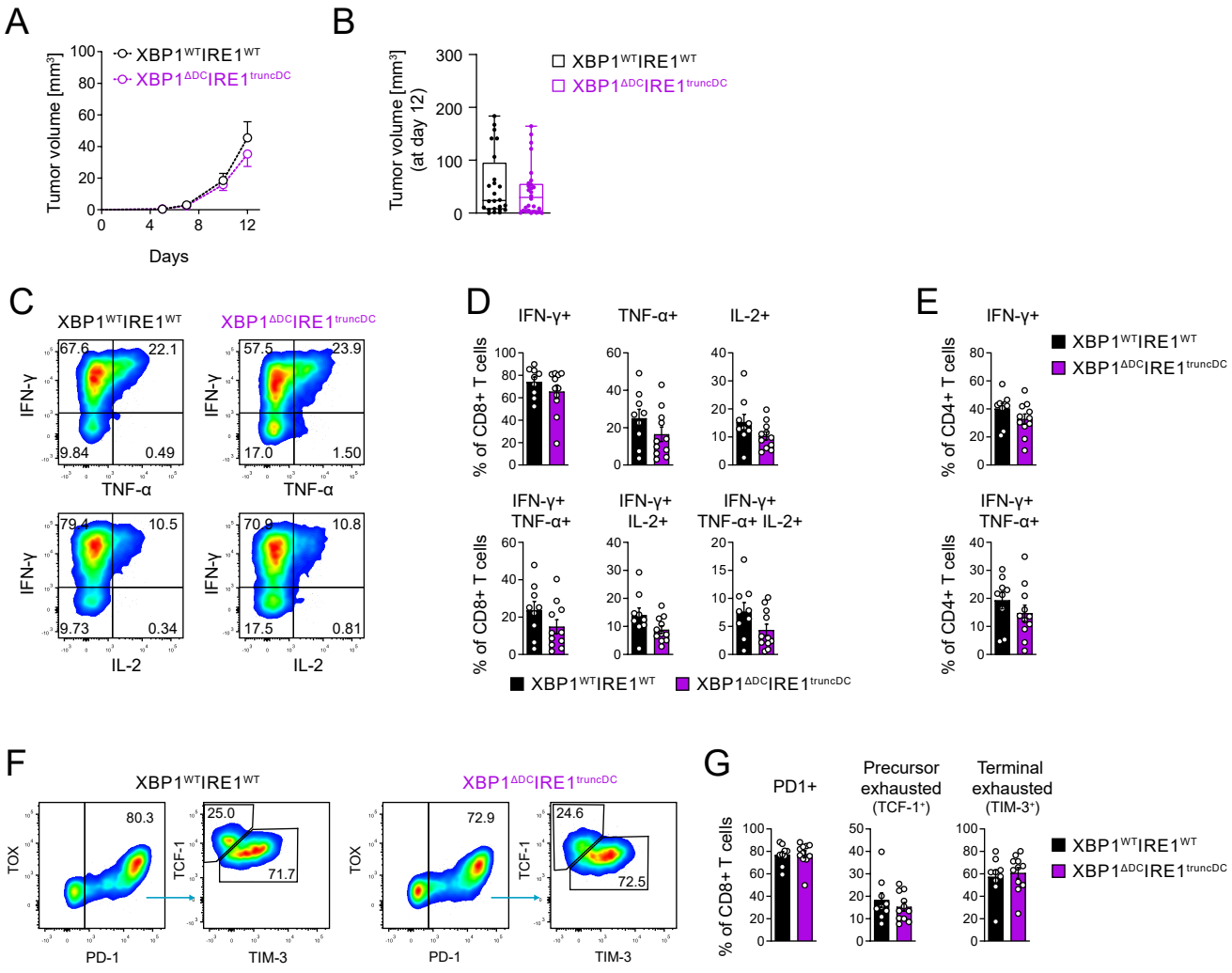
A
B
C
D
E
F
G
XBP1WTIRE1WT
XBP1ΔDCIRE1truncDC
Tumor volume [mm3]
Days
Tumor volume [mm3] (at day 12)
IFN-γ
TNF-α
IL-2
67.6
22.1
9.84
0.49
57.5
23.9
17.0
1.50
79.4
10.5
9.73
0.34
70.9
10.8
17.5
0.81
IFN-γ+
TNF-α+
IL-2+
IFN-γ+ TNF-α+
IFN-γ+ IL-2+
IFN-γ+ TNF-α+ IL-2+
% of CD8+ T cells
% of CD4+ T cells
TOX
PD-1
TCF-1
TIM-3
80.3
25.0
71.7
72.9
24.6
72.5
PD1+
Precursor exhausted (TCF-1+)
Terminal exhausted (TIM-3+)